Prandtl number dependence of stratified turbulence

by

Jesse Danielle Legaspi

A thesis
presented to the University of Waterloo
in fulfillment of the
thesis requirement for the degree of
Master of Mathematics
in
Applied Mathematics

Waterloo, Ontario, Canada, 2019

Author's Declaration

I hereby declare that I am the sole author of this thesis. This is a true copy of the thesis, including any required final revisions, as accepted by my examiners.

I understand that my thesis may be made electronically available to the public.

Abstract

Stratified turbulence is affected by buoyancy forces that suppress vertical motion, resulting in a horizontally-layered structure with quasi-two-dimensional vortices. The Prandtl number Pr quantifies the relative strengths of viscosity and buoyancy diffusivity, which damp small-scale fluctuations in velocity and buoyancy at different microscales. Direct numerical simulations (DNS) must resolve the smallest flow features, requiring very high resolution if Pr is large. In most oceanic and atmospheric flows, $Pr > 1$; e.g. $Pr = 7$ in heat-stratified water, and $Pr = 700$ in salt-stratified water. To reduce the computational demand in simulations of ocean flows and lab experiments of stratified turbulence, $Pr = 1$ is often assumed, possibly introducing discrepancies between the DNS and real geophysical stratified turbulence. In this thesis, we explore how stratified turbulence is affected by varying Pr. DNS of homogeneous forced stratified turbulence with a fixed viscosity and $Pr = 0.7$, 1, 2, 4, and 8 are performed for different stratification strengths by changing the buoyancy frequency N, for a range of Froude numbers Fr_h from 0.009 to 0.1, and buoyancy Reynolds numbers Re_b from 0.5 to 32. Energy spectra, buoyancy flux spectra, spectral energy flux, and snapshots of physical space fields are compared as Pr increases to explore scale-specific Pr-sensitivity. Probability density functions and statistical moments of velocity component and temperature derivative fields are also compared to the $Pr = 1$ findings. Small-scale Pr-dependence was found in the kinetic energy spectra that extended further upscale as stratification increased. The potential energy and potential energy flux exhibited more prominent Pr-sensitivity, extending into the large horizontal scales for some stratifications. Interestingly, the kinetic energy flux exhibited no Pr-dependence at small scales. The buoyancy flux was most sensitive to Pr in the small scales, except for the most strongly stratified case, which notably had $Re_b < 1$. As Pr increased, all spectra showed a pattern of diminishing increase, suggesting eventual convergence to a limiting spectra shape at large but finite Pr. The spectra in the most strongly stratified case, where $Re_b < 1$, were very different from the rest, suggesting regime-dependence of Pr-sensitivity (i.e. whether $Re_b < 1$, or $Re_b > 1$). The probability density functions and statistical moments for Pr different from 1 were consistent with previous work for $Pr = 1$. Increasing Pr significantly affected the temperature derivative fields while the velocity component derivative fields were mostly unchanged. These findings suggest that, for DNS of stratified turbulence in fluids with $Pr > 1$, the assumption of $Pr = 1$ does not produce realistic results: the Pr-sensitivity at intermediate, and in some cases, large horizontal scales must be considered for accurate stratified turbulence DNS, though the excessive computational demand can be prohibitive.

Acknowledgements

Thank you to Michael Waite for his supervision, patience, and guidance. The completion of this work is owed to Mike's availability, quick feedback, and regular meetings that helped keep me on track. I'm grateful to have learned so much over the past 2 years – thank you for taking me on as a graduate student!

Thank you to Marek Stastna and Francis Poulin for their time spent reviewing my work and for their ideas on extending this research.

Thanks also to Tom Russell and Cathy Christie at Queen's University for helping me return to UW.

I would not have made it this far without my officemates (in no particular order): Christian Barna, Josh Thompson, Tim Dockhorn, Rishi Chakraborty, and unofficial officemate Stan Zonov. Thank you guys for your friendship and good humour – the office won't be the same after you all move on!

To the past and present fluids lab members and to my other AMATH peers, thank you for your help along the way.

Thank you to Jeremy Roth for helping me find my strength over the past year, and also to the rest of the team for keeping a fun and positive atmosphere.

Eric Silva, thanks for the support from afar!

Ken Chadwick, thank you for your endless love.

This work was enabled in part by the computing resources provided by SHARCNET and Compute Canada.

Dedication

To Lola, Lolo, and my good boy Shadow.

Table of Contents

List of Tables

List of Figures

Chapter 1

Introduction

1.1 Stratified turbulence and the Prandtl number

In the turbulent flows of the atmosphere and ocean, buoyancy forces and stable stratification restrict vertical motion. At sufficiently small scales, the effects due to rotation are minor: stratification dominates these scales while Coriolis forces are weak [Riley and Lindborg, 2013]. Fluid velocities in stratified turbulence are approximately horizontal and layers containing quasi-two-dimensional vortices develop [Waite, 2014], along with gravity waves [Staquet and Sommeria, 2002]. At very small scales, fluctuations of variable fields (e.g. velocity, vorticity, density, temperature, etc.) are smoothed out by viscosity and buoyancy diffusivity, which typically occur at different inner scales. Direct numerical simulations (DNS) of stratified turbulence require that the smallest features are resolved, necessitating adequately fine grid spacing. The computational cost for these DNS is often reduced by assuming the two smoothing processes to be equally strong, but is done at the expense of misrepresenting the two disparate inner scales.

The relative strength of viscosity and buoyancy diffusivity is quantified by the dimensionless Prandtl number

$$Pr \equiv \nu/\kappa, \tag{1.1}$$

for kinematic viscosity ν and thermal diffusivity κ, with temperature as the buoyancy-influenced scalar. Typical values for Pr are 0.7 for heat in air and 7 for heat in water; for salinity in water the analogous Schmidt number for ratio of viscosity to mass diffusivity is about 700. We use Pr in this thesis to refer to this ratio. Using large Pr values for DNS

is computationally expensive: since buoyancy diffusivity can be several times weaker than viscous diffusion, the smallest temperature fluctuations can be reduced to extremely small scales, demanding high spatial resolution. By setting $Pr = 1$, the equally strong viscous dissipation and buoyancy diffusivity forces the two inner scales to coincide, relaxing the need for high resolution. Stratified turbulence dynamics could be sensitive to Pr, but the $Pr \neq 1$ problem has not been studied in depth for these types of flows. In this paper, we investigate the effect of varying Pr in numerical simulations of homogeneous stratified turbulence and evaluate the soundness of the $Pr = 1$ approximation.

1.1.1 The energy cascade

Some preliminary concepts from classical turbulence theory are briefly introduced here, following from Kundu et al. [2012] and Davidson [2015]. Richardson [1922] proposed that in turbulent flows, the kinetic energy follows a cascade from large to small eddies (or vortices) until it is destroyed by viscous dissipation. Turbulence is characterized by a large Reynolds number,

$$Re = ul/\nu, \tag{1.2}$$

where u is a large-scale velocity and l is the large eddy length scale. The Reynolds number measures the relative strength of inertial forces to viscous forces. Energy-containing eddies of size l are not significantly affected by viscosity in high-Re turbulence, since $ul/\nu \gg 1$. These large eddies transfer their energy to slightly smaller eddies through vortex stretching and tilting, which in turn pass energy to smaller eddies, and so on until the eddies are small enough that viscous effects become important. The kinetic energy is then dissipated at a rate ϵ_k, for which a good approximation is [Taylor, 1935]

$$\epsilon_k \sim u^3/l. \tag{1.3}$$

The inertial subrange describes the range of length scales where this cascade takes place, driven only by inertial forces. In homogeneous, statistically stationary turbulence, this energy cascade rate is constant and equal to ϵ_k.

The kinetic and potential energy can be studied in terms of their spectra (i.e. as a function of three-dimensional wavevectors $\vec{k}$) to identify scale-specific contributions to the energy. That is, the kinetic energy KE over a sphere of radius $k = |\vec{k}|$ can be expressed as [Wyngaard, 2010]

$$KE = \int_0^\infty E_K(k)\ \mathrm{d}k, \tag{1.4}$$

where $E_K(k)$ is its three-dimensional spectrum, and likewise for potential energy PE,

$$PE = \int_0^\infty E_P(k)\ \mathrm{d}k, \tag{1.5}$$

with its three-dimensional spectrum $E_P(k)$. Based on dimensional analysis, Kolmogorov [1941] predicted the form of the kinetic energy spectrum in the inertial subrange to be

$$E_K \sim \epsilon_k^{2/3} k^{-5/3}, \tag{1.6}$$

in which the spectrum depends only on ϵ_k and wavenumber k. Similarly, for the spectrum of the potential energy, Obukhov [1949] and Corrsin [1951] proposed the form

$$E_P \sim \frac{\epsilon_p}{\epsilon_k^{1/3}} k^{-5/3}, \tag{1.7}$$

where ϵ_p is the potential energy dissipation rate. With these scaling arguments, log-log plots of $E_K(k)$ and $E_P(k)$ are expected to have a slope of -5/3 in the inertial range. Downscale of the inertial range, corresponding to larger k, the spectrum would steepen significantly as the energy at small scales is destroyed by viscous dissipation.

The spectral fluxes $\Pi_K(k)$ and $\Pi_P(k)$ of kinetic and potential energy respectively measure the rate at which energy is transferred through wavenumber k [Lindborg, 2006, Davidson, 2015]. A positive spectral flux corresponds to the forward cascade of energy from small k to large k, which is from large length scales to small length scales. In an inertial subrange, both $\Pi_K(k)$ and $\Pi_P(k)$ exhibit positive plateau. More details on the spectral flux follow in Secs. 2.1.3 and 3.2.3.

1.1.2 Characteristic scales and numbers

Stratified turbulence is characterized by several length scales and dimensionless numbers, which we begin to review here [Riley and Lelong, 2000, Riley and Lindborg, 2013, Davidson, 2013]. The Kolmogorov microscale

$$k_d \equiv (\epsilon_k/\nu^3)^{1/4}, \tag{1.8}$$

is the inner scale of velocity fluctuations where kinetic energy is viscously dissipated into heat [Kolmogorov, 1941]. Analogous to the viscous dissipation scale, the temperature fluctuations, θ, have inner scale [Corrsin, 1951, Tennekes and Lumley, 1972]

$$k_\theta \equiv (\epsilon_k/\kappa^3)^{1/4}, \tag{1.9}$$

for thermal diffusion. There is also the Batchelor scale for the inner scale that describes passive scalar fluctuations [Batchelor, 1959, Davidson, 2015]

$$k_B \equiv (\epsilon_k/\nu\kappa^2)^{1/4}. \tag{1.10}$$

These two inner temperature scales are related by

$$k_\theta/k_B = (\nu/\kappa)^{1/4} = Pr^{1/4}. \tag{1.11}$$

Depending on the size of Pr, either k_θ or k_B describes the dissipation scale for potential energy. When $Pr \lesssim 1$, k_θ is most applicable, and when $Pr \gg 1$, k_B is most applicable [Wyngaard, 2010, Gotoh and Yeung, 2013]; we will focus on k_θ as the inner temperature scale. When $Pr > 1$, we have that $k_\theta > k_d$, meaning that viscosity will begin to destroy velocity fluctuations at a scale where buoyancy diffusivity will not yet be effective. This subrange $k \in [k_d, k_\theta]$ is referred to as the viscous-convective subrange. If $Pr \gg 1$, theory suggests that in the viscous-convective subrange, the potential energy spectrum has the form

$$E_P \sim \epsilon_p(\epsilon_k/\nu)^{-1/2}k^{-1}, \tag{1.12}$$

as predicted by Batchelor [1959]. In the opposite case when $Pr < 1$, buoyancy diffusivity will act on small scales where viscous effects are not yet significant, and the subrange $k \in [k_\theta, k_d]$ is called the inertial-diffusive subrange [Wyngaard, 2010]. In the atmosphere, these inner scales typically correspond to lengths on the order of millimeters.

The buoyancy frequency N characterizes stratification strength: for temperature stratification,

$$N^2 \equiv \frac{g}{\theta_0}\beta, \tag{1.13}$$

where g is gravitational acceleration, θ_0 is a reference temperature, and β is the background potential temperature gradient [Kundu et al., 2012]. The diffusion of temperature fluctuations can be related to the potential energy dissipation rate by

$$2\kappa\frac{\partial\theta}{\partial x_j}\frac{\partial\theta}{\partial x_j} = \frac{\epsilon_p}{N}. \tag{1.14}$$

The potential temperature fluctuations θ refers to a fluid particle's change in temperature following an adiabatic displacement to a reference pressure [Tritton, 1988, Kundu et al., 2012]; in this thesis, we make the Boussinesq approximation (Sec. 2.1.1) for which temperature and potential temperature are equivalent [Tritton, 1988].

The $Pr \neq 1$ problem in strongly stratified turbulence becomes complicated by the horizontally-layered flow. In stratified turbulence, the quasi-two-dimensional vortices become thinner with stronger stratification [Billant and Chomaz, 2001], introducing additional small scales that must be adequately resolved in DNS. The horizontal Froude number

$$Fr_h = U/NL_h, \tag{1.15}$$

for rms velocity U and horizontal length scale L_h, is a dimensionless number that quantifies stratification strength in stratified turbulence [Billant and Chomaz, 2001, Brethouwer et al., 2007]. While turbulence is characterized by a large Reynolds number

$$Re = UL_h/\nu, \tag{1.16}$$

(the same definition as in equation (1.2) but with the horizontal length scale) stratified turbulence can fall into one of two regimes depending on its buoyancy Reynolds number [Brethouwer et al., 2007, Waite, 2014]

$$Re_b = ReFr_h^2. \tag{1.17}$$

For typical troposphere values $U \sim 1$ ms^{-1}, $L_h \sim 100$ km, $N \sim 10^{-2}$ s^{-1}, and $\nu \sim 10^{-5}$ m^{2}s^{-1}, these dimensionless numbers are approximately $Fr_h \sim 10^{-3}$, $Re \sim 10^{10}$, and $Re_b \sim 10^4$ [Waite, 2013]. From the approximation in (1.3), these values give a corresponding $\epsilon_k \sim 10^{-5}$ m^{2}s^{-3} (similar to dissipation values in the stratosphere [Dewan, 1997]).

Stratified turbulence also has the buoyancy scale

$$k_b \equiv N/U, \tag{1.18}$$

and Ozmidov scale

$$k_O \equiv (N^3/\epsilon_k)^{1/2}, \tag{1.19}$$

which characterize different small-scale processes in the flow. The thickness of the horizontal layers in stratified turbulence, and thus the largest vertical overturning scale corresponds to k_b [Carnevale et al., 2001, Billant and Chomaz, 2001, Waite and Bartello, 2004]. The Ozmidov scale is the largest scale for which the flow resembles small-scale three-dimensional isotropic turbulence [Ozmidov, 1965]. Whether k_O is upscale or downscale of the dissipation range depends on the regime of stratified turbulence, such that

$$k_d/k_O \sim Re_b^{3/4}, \tag{1.20}$$

using the assumption that $\epsilon_k \sim U^3/L_h$ [Lindborg, 2006, Maffioli and Davidson, 2016].

1.1.3 Previous results in stratified turbulence

Past investigations that used the $Pr = 1$ approximation revealed important properties of stratified turbulence and confirmed various scaling arguments. Stratified turbulence has two regimes: on the scale of the thickness of the quasi-two-dimensional vortices, viscosity may be weak enough that small eddies may emerge and the layers are turbulently coupled (characterized by $Re_b > 1$), or viscosity may be strong enough that the layers are non-turbulent and become viscously coupled (characterized by $Re_b < 1$) [Riley and de Bruyn Kops, 2003, Brethouwer et al., 2007]. Within the horizontal layers, Kelvin-Helmholtz (KH) instabilities emerge when $Re_b \gtrsim 1$ and break down into small-scale turbulence [Lilly, 1983, Riley and de Bruyn Kops, 2003, Laval et al., 2003, Brethouwer et al., 2007, Waite, 2011]. The kinetic and potential energy spectra in terms of horizontal wavenumber k_h and vertical wavenumber k_v have been extensively examined in studies with stratified turbulence simulations. Forced simulation results have shown the horizontal kinetic and potential energy spectra to exhibit $k_h^{-5/3}$ scaling [Lindborg, 2006, Brethouwer et al., 2007, Almalkie and de Bruyn Kops, 2012]. In some instances, there is a noticeable bump at $k_h \sim k_b$ due to KH instabilities [Laval et al., 2003, Brethouwer et al., 2007, Waite, 2011]. Scaling arguments have suggested k_v^{-3} scaling for the vertical kinetic and potential energy spectra for a limited range of wavenumbers [Billant and Chomaz, 2001, Lindborg, 2006]; simulations have exhibited similarly steep vertical spectra past k_b [Waite and Bartello, 2004, Brethouwer et al., 2007, Almalkie and de Bruyn Kops, 2012]. The behaviour of vertical spectra is scale-dependent: at large horizontal scales, agreement with k_v^{-3} scaling was shown for both kinetic and potential energy, but for different ranges of wavenumbers in simulations forced at large scales [Maffioli, 2017]. Decaying simulations also supported the horizontal $k_h^{-5/3}$ scaling for kinetic and potential energy found in forced simulations [Bartello and Tobias, 2013, Maffioli and Davidson, 2016], and were not influenced by stratification strength for large Re [Lindborg, 2006, Bartello and Tobias, 2013]. The conversion from potential to kinetic energy can be quantified by the buoyancy flux term in the energy budget [Holloway, 1988, Waite, 2014]. In the buoyancy flux spectrum, restratification describes the small-scale subrange with positive buoyancy flux, where potential energy is converted to vertical kinetic energy, restratifying the flow [Holloway, 1988].

Stratified turbulence with $Pr > 1$ has not been as well-studied as the $Pr = 1$ case, but previous studies have analyzed such simulations with some compromises in other simulation parameters. A recent study which compared $Pr = 7$ and $Pr = 700$ DNS of decaying stratified turbulence revealed Pr-dependence in the energy spectra [Okino and Hanazaki, 2017]. The $Pr = 700$ potential energy spectra initially exhibited k^{-1} scaling at large wavenumbers (as predicted in the viscous-convective subrange for passive scalars [Batchelor, 1959]), and

by the final decay period, a flat spectrum developed in the dissipation range. However, the initial Reynolds number in this study was necessarily small ($Re = 50$) to accommodate the very large Pr, limiting the extent of the inertial range; while small-scale changes due to Pr have been identified, it is also of interest to determine any possible Pr-dependence upscale of the dissipation range. An older study which performed DNS of stably stratified homogeneous turbulent shear flow concluded higher-Pr flows were more likely to exhibit counter-gradient heat flux (i.e. restratification [Holloway, 1988]) in the vertical direction, but their moderate Re limits its applicability to geophysical flows [Gerz et al., 1989]. Another study where DNS of density-stratified turbulent wakes were performed for $Pr = 0.2$, 1, and 7 concluded that using the $Pr = 1$ assumption for the $Pr = 7$ case was reasonable, though the grid spacing was four times the smallest length scale of the flow [de Stadler et al., 2010]. The $Pr = 7$ case induced small-scale changes with little influence on the wake's large-scale features, and the differences between the $Pr = 1$ and $Pr = 7$ cases were small compared to the substantial difference in computational costs.

Since varying Pr affects the relative strengths of small-scale processes, we anticipate that most Pr-induced changes will occur around the small viscous dissipation and buoyancy diffusion scales. If the viscosity is held fixed while Pr is increased, we would also predict that changes in the temperature and potential energy are more exaggerated than in the velocity and kinetic energy. Further, for fixed viscosity, the dissipation of potential energy (or of temperature fluctuations, as in equation (1.14)) is expected to be especially Pr-sensitive as k_θ is modified. Equation (1.20) expresses a scale separation in stratified turbulence in terms of the characteristic Re_b, forecasting that sensitivity to Pr may depend on the regime of stratified turbulence. As a small-scale phenomenon involving the flow's potential energy, restratification is another candidate for Pr-dependence. Due to the complicated dependence of buoyancy flux on the stratification strength, varying Pr may also affect the restratification range in regime-specific ways [Lucas et al., 2017].

1.2 Stratification and isotropy

In de Bruyn Kops [2015], four DNS were performed (one homogeneous isotropic benchmark, and three of axisymmetric forced homogeneous turbulence with different stratification strengths) to investigate the extent to which strongly stratified turbulence satisfies classical scaling arguments by Kolmogorov, Obukhov, and Corrsin (KOC scaling), and for their agreement with related theory on local isotropy, the lognormal model for energy dissipation, structure functions of velocity and scalar fields, local dissipation rates, internal intermittency, and velocity and scalar exponents of internal intermittency. In this thesis,

we consider the dependence of these local isotropy results on Pr.

Excluding the isotropic benchmark case, stratification strength was increased by decreasing Fr_h to obtain values of $Fr_h = 1.0$, 0.52, and 0.26, with associated values of $Re_b = 220$, 48, and 13, respectively. The stratified simulations in de Bruyn Kops [2015] all used the $Pr = 1$ simplification and were resolved on cuboid domains with $8192 \times 8192 \times 4096$ grid points. The buoyancy Reynolds numbers span a value of 30: this was intentional, due to the hypotheses that flows must have $Re_b \approx 30$ so that active turbulence forms [Gibson, 1980, de Bruyn Kops, 2015].

KOC scaling refers to the classical scaling arguments in Kolmogorov [1941], Obukhov [1941a,b, 1949], Corrsin [1951], Kolmogorov [1962], Obukhov [1962]. Two principal assumptions common to KOC scaling hypotheses are adequate scale separation and local isotropy. Adequate scale separation, desirable for studying strongly stratified turbulence DNS, is related to a large Re_b as noted above in equation (1.20). One indicator of anisotropy is the skewness of the scalar (e.g. temperature) derivatives: nonzero skewness of scalar derivatives parallel to the mean gradient (e.g. the vertical direction in these stratified flows) indicate scalar anisotropy at small scales [Gibson et al., 1970]. Stratified turbulence by definition has a mean scalar gradient so that local isotropy cannot be satisfied. However, isotropic homogeneous turbulence with a mean gradient in a scalar still manages to exhibit KOC scaling in that scalar, despite its anisotropic local scalar derivatives [Almalkie and de Bruyn Kops, 2012, de Bruyn Kops, 2015]. Specific to simulations in de Bruyn Kops [2015], KOC scaling was observed only in the case with weakest stratification, $Fr_h = 1.0$, corresponding to the case with the largest $Re_b = 220$. However, these observations were made with $Pr = 1$, so these results might not reflect the outcome of unequal viscous and thermal diffusivity processes. To extend this study, physical space fields and their derivatives are analyzed with the same approach as de Bruyn Kops [2015], but for simulations with $Pr = 0.7$, 1, 2, and 4 and stratification strengths $N = 0.075$, 0.15, 0.3, and 0.6. Probability density functions and statistical moments are analyzed for these simulations to explore the possible effect of Pr on their measures of isotropy.

1.3 Format of thesis

This thesis includes findings from (a) the main investigation of Pr-dependence in stratified turbulence spectra and physical fields, and (b) the results of an earlier project that expanded on the study reviewed in Sec. 1.2 by de Bruyn Kops [2015], by using $Pr \neq 1$ simulations on a smaller scale. The same simulations for $Pr = 0.7$, 1, 2, and 4 are used in both parts, but the $Pr = 8$ simulations had not been performed until after project (b)

was completed. Ultimately, both parts explore the open question of Pr-dependence in stratified turbulence. The choices of Pr and N span a range of Re_b so that the $Re_b = 1$ stratified turbulence regime transition may also be studied. In Chapter 2, the numerical model, equations, and setup of simulations are explained. In Chapter 3, the simulation results are analyzed in terms of scale-specific observations of Pr-dependence in the energy spectra, buoyancy flux spectra, spectral energy flux, and snapshots of physical space fields. Conclusions, discussion, and future work are given in Chapter 4.

Chapter 2

Methodology

2.1 Equations and model

2.1.1 The Boussinesq equations

For the stratified turbulence simulations presented here, the governing equations are the uniformly stratified Boussinesq equations on an f-plane in three dimensions:

$$\frac{\mathrm{D}\vec{u}}{\mathrm{D}t} + f\vec{z} \times \vec{u} = -\nabla p + \alpha\theta\hat{z} + \vec{F}_u + \nu\nabla^2\vec{u}, \tag{2.1}$$

$$\frac{\mathrm{D}\theta}{\mathrm{D}t} + \beta w = F_b + \kappa\nabla^2\theta, \tag{2.2}$$

$$\nabla \cdot \vec{u} = 0, \tag{2.3}$$

where $\vec{u}$ is velocity, f is the Coriolis parameter, p is pressure scaled by a reference density, θ is the potential temperature fluctuation (or negative density fluctuation), $\vec{F}_u$ is the velocity forcing, F_b is the temperature forcing, ν is viscosity, κ is diffusivity, α is thermal expansivity, and β is the background potential temperature gradient [Herring and Métais, 1989].

The Boussinesq approximation is described in introductory fluids textbooks, e.g. Chapter 14 in Tritton [1988] and Chapter 4 in Kundu et al. [2012], and is commonly used for geophysical flows. Provided that θ is sufficiently small, it appears only in the second term on the right hand side of equation (2.1) to reflect that the fluctuations are most important in their contributions to the buoyancy force [Davidson, 2013]. Other than for the buoyancy force, density fluctuations are ignored and the fluid is treated as incompressible. For

the Boussinesq approximation to hold, it is assumed that the Mach number of the flow is small, frequencies are slow compared to the acoustic frequency, and vertical scales are smaller than the density scale height [Kundu et al., 2012]. A small Mach number (the ratio of U to the speed of sound in the medium) limits fluid velocities such that the density variations induced by velocity divergence are negligible. Pressure variations attributed to propagating sound waves may be neglected if the frequencies of small perturbations are slow compared to the fluid's acoustic frequency. A small vertical scale ensures that hydrostatic changes in pressure do not cause significant changes in density. Small-scale geophysical turbulence satisfies all of these assumptions.

To simplify the problem of studying geophysical flows for a rotating Earth, we can consider the tangent plane at a particular latitude and use a Cartesian coordinate system, provided that the horizontal length scales are much smaller than Earth's radius [Kundu et al., 2012]. Further, the f-plane model assumes that f, which accounts for rotation of the Earth, is a constant value that does not change with latitude. This assumption requires that the time and length scales are not very long (several weeks, or thousands of kilometers) [Kundu et al., 2012]. Rotational effects can optionally be considered in this setup, but for the simulations presented here the effects of rotation and the term in equation (2.1) including f will be ignored.

2.1.2 Numerical method

The DNS code computes the fluid velocity by first solving for vorticity ($\vec{\omega} = \nabla \times \vec{u}$) from the vorticity formulation of (2.1):

$$\frac{\partial \vec{\omega}}{\partial t} = \nabla \times (\vec{u} \times \vec{\omega}) + \alpha \begin{bmatrix} \partial\theta/\partial y \\ -\partial\theta/\partial x \\ 0 \end{bmatrix} + \vec{F}_\omega + \nu \nabla^2 \vec{\omega}, \tag{2.4}$$

and (2.2), then inverting the result for $\vec{u}$. This inversion assumes no mean velocity. In this formulation, the second term on the right hand side of (2.4) corresponds to the baroclinic generation of vorticity, and $\vec{F}_\omega = \nabla \times \vec{F}_u$ is the vorticity forcing.

The spectral transform method is used on a triply periodic domain to solve the uniformly stratified Boussinesq equations (2.2), (2.3), and (2.4). The domain is a cube of size $L \times L \times L$ and grid size $n \times n \times n$ in both the physical and Fourier domains where $\vec{u}$, $\vec{\omega}$, and θ are stored. Nonlinear terms are computed in the physical domain, and spatial derivatives are computed in the Fourier domain, and a Fast Fourier Transform is used to go between domains [Frigo and Johnson, 2005]. Third-order Adams-Bashforth time stepping is used

with constant time step Δt, and viscous and diffusive terms use a Crank-Nicolson scheme [Durran, 2010]. Aliasing issues are countered by a less restrictive wavenumber truncation than the 2/3 rule, which is known to eliminate all aliasing error [Durran, 2010]. Previous DNS studies have used wavenumber truncations as high as 15/16, which still managed to remove the dominant aliasing error [Riley and de Bruyn Kops, 2003]. In the following simulations, the Fourier coefficients are spherically truncated at a maximum wavenumber $k_{max} = (\frac{n}{2})(\frac{8}{9}) = 4n/9$. The effective resolution is then $\Delta x = \Delta y = \Delta z = 9L/8n$ with wavenumber spacing $\Delta k_x = \Delta k_y = \Delta k_z = 2\pi/L$. This model has been used in numerous studies of stratified turbulence, e.g. Waite [2011, 2017], Lang and Waite [2019].

2.1.3 Energy budget equations

The equations for the kinetic and potential energy budget for each wavevector $\vec{k}$ are:

$$\frac{\partial E_K}{\partial t}(\vec{k}) = T_K(\vec{k}) + B(\vec{k}) - D_K(\vec{k}) + F(\vec{k}), \tag{2.5}$$

$$\frac{\partial E_P}{\partial t}(\vec{k}) = T_P(\vec{k}) - B(\vec{k}) - D_P(\vec{k}). \tag{2.6}$$

The first terms on the right hand side of (2.5)-(2.6),

$$T_K(\vec{k}) \equiv -\mathrm{Im} \sum_{\vec{k}+\vec{p}+\vec{q}=0} P_{ijm}(\vec{k})\hat{u}_j(\vec{p})\hat{u}_m(\vec{q})\hat{u}_i(\vec{k}), \tag{2.7}$$

$$T_P(\vec{k}) \equiv -\frac{\alpha}{\beta}\mathrm{Im}\left(k_j \sum_{\vec{k}+\vec{p}+\vec{q}=0} \hat{\theta}(\vec{k})\hat{\theta}(\vec{p})\hat{u}_j(\vec{q}) \right), \tag{2.8}$$

are the nonlinear kinetic and potential energy transfer respectively, using standard projection operator P_{ijm} [Rose and Sulem, 1978]. The buoyancy flux, B, is

$$B(\vec{k}) \equiv \alpha \mathrm{Re}\Big(\hat{\theta}(\vec{k})\hat{w}^*(\vec{k})\Big), \tag{2.9}$$

the kinetic and potential energy dissipation are

$$D_K(\vec{k}) \equiv 2\nu k^2 E_K(\vec{k}), \tag{2.10}$$

$$D_P(\vec{k}) \equiv 2\kappa k^2 E_P(\vec{k}), \tag{2.11}$$

and F is the forcing. Horizontal and vertical components of (2.5)-(2.6) are found by summing over all wavevectors $\vec{k}$ for particular k_h or k_v.

The buoyancy flux B is the cross spectrum of buoyancy and vertical velocity, and can be interpreted as the transfer of potential to kinetic energy [Holloway, 1988, Waite, 2014]. To justify restratification, Holloway [1988] suggested that the downscale transfer of potential energy to small scales was more efficient than for kinetic energy, leading to a tendency for more potential energy than kinetic energy to accumulate at small scales. Oppositely, more kinetic energy would accumulate at large scales than potential energy, and so these imbalances drive the conversion of kinetic to potential energy at large scales ($B < 0$) and potential to kinetic energy at small scales ($B > 0$, restratification).

The transfer terms represent the conservative transfer of potential and kinetic energy to different wavenumbers. Since they are conservative, the spectral fluxes of kinetic and potential energy are obtained from the transfer terms as

$$\Pi_K(k) = -\int_0^k T_K(k)\ \mathrm{d}k, \tag{2.12}$$

$$\Pi_P(k) = -\int_0^k T_P(k)\ \mathrm{d}k. \tag{2.13}$$

As conserved quantities, the transfer terms satisfy

$$\int_0^\infty T_K(k)\ \mathrm{d}k = 0 \text{ and } \int_0^\infty T_P(k)\ \mathrm{d}k = 0, \tag{2.14}$$

which also manifest as $\Pi_K = 0$ and $\Pi_P = 0$ at k_{max}.

2.2 Simulation setup

The parameter values, nondimensional numbers, and wavenumbers for all simulations presented here are given in Table 2.1. These simulations are performed on cubic domains of size $L = 2\pi$ with $n = 1536$ grid points in each direction. The total integration length across all simulations is 500 time units and the time step is $\Delta t = 0.00625$. Energy time series, energy dissipation time series, energy spectra, and energy transfer spectra are output every 10 time units in each simulation.

The horizontal and vertical kinetic energy spectra are [Waite and Bartello, 2004]

$$E_K(k_h)\delta = \frac{1}{2}\sum_{\vec{k'}\in I_h(k_h)} |\hat{\vec{u}}(\vec{k'})|^2, \tag{2.15}$$

$$E_K(k_v)\delta = \frac{1}{2}\sum_{\vec{k'}\in I_v(k_v)} |\hat{\vec{u}}(\vec{k'})|^2, \tag{2.16}$$

Run	N	Pr	Fr_h	Re	Re_b	$\epsilon_k(\times 10^{-6})$	$\epsilon_p(\times 10^{-6})$	k_d	k_θ	k_{max}/k_d	k_{max}/k_θ	k_O	k_b
A0	0.075	0.7	0.0911	3310	27.5	1.85	1.02	181	138	3.77	4.92	15	5
A1	0.075	1	0.0947	3197	28.7	1.93	0.977	183	183	3.73	3.73	15	5
A2	0.075	2	0.0983	3094	29.9	2.02	0.863	185	311	3.69	2.19	14	5
A3	0.075	4	0.103	2941	31.2	2.11	0.788	187	528	3.65	1.29	14	5
A4	0.075	8	0.106	2839	31.7	2.14	0.713	188	892	3.64	0.76	14	5
B0	0.15	0.7	0.0402	4304	6.94	1.87	1.03	181	139	3.76	4.91	42	9
B1	0.15	1	0.0420	4130	7.28	1.97	0.920	184	184	3.71	3.71	41	8
B2	0.15	2	0.0452	3877	7.92	2.14	0.763	188	315	3.64	2.16	40	8
B3	0.15	4	0.0479	3658	8.38	2.26	0.627	190	538	3.59	1.27	39	8
B4	0.15	8	0.0499	3491	8.71	2.35	0.529	192	914	3.55	0.75	38	8
C0	0.3	0.7	0.0191	5279	1.93	2.09	1.03	186	143	3.66	4.78	114	16
C1	0.3	1	0.0201	5041	2.03	2.19	0.908	189	189	3.61	3.61	111	16
C2	0.3	2	0.0218	4670	2.22	2.40	0.688	193	325	3.53	2.10	106	16
C3	0.3	4	0.0233	4381	2.37	2.56	0.514	196	555	3.48	1.23	103	16
C4	0.3	8	0.0244	4179	2.49	2.69	0.384	199	945	3.43	0.72	100	16
D0	0.6	0.7	0.00896	6737	0.541	2.34	0.888	192	147	3.56	4.65	304	29
D1	0.6	1	0.00935	6485	0.567	2.45	0.780	194	194	3.52	3.52	297	29
D2	0.6	2	0.0101	6045	0.613	2.65	0.571	198	333	3.45	2.05	286	29
D3	0.6	4	0.0107	5674	0.654	2.82	0.394	201	569	3.39	1.20	277	29
D4	0.6	8	0.0112	5423	0.684	2.95	0.263	203	967	3.35	0.71	270	29

Table 2.1: Simulation parameters, nondimensional numbers, and wavenumbers for all simulations. The run label letter A/B/C/D indicates a common buoyancy frequency. The run label number 0/1/2/3/4 indicates a common Prandtl number. All simulations have the same viscosity, resolution, and maximum wavenumber: $\nu = 1.2 \times 10^{-5}$, $n = 1536$, $k_{max} = 682$.

where

$$I_h(k_h) = \{\vec{k'} \mid k_h - \delta/2 \leq k'_h < k_h + \delta/2\}, \tag{2.17}$$

$$I_v(k_v) = \{\vec{k'} \mid k_v - \delta/2 \leq |k'_v| < k_v + \delta/2\}, \tag{2.18}$$

$\delta = 2\pi/L$, and $\hat{\vec{u}}$ corresponds to the velocity in the Fourier domain. For $n = 1536$ gridpoints, the spectra are computed for $k_h \in [0, 964]$ and $k_v \in [0, 682]$. The additional k_h components come from corner regions outside the circle of radius $k_{max} = 682$ in a horizontal plane. The horizontal and vertical potential energy spectra are similarly defined.

The time series are used for the calculated values in Table 2.1, based on values for ϵ_k and ϵ_p averaged over the last 200 simulation time units. The length scale used in Fr_h and Re is computed from $L_h = U^3/\epsilon_k$, where U is the root mean square velocity (as in [Brethouwer et al., 2007]). Velocity, vorticity, and temperature fields in physical space are output at equidistant times over the integration length (either 5 or 9 output times depending on the case). With this setup, the last performed simulation was run D4, which took 78.06 hours on 768 processors on Cedar.

Large-scale vortical modes are randomly forced by directly forcing rotational velocity in these strongly stratified simulations [Waite and Bartello, 2004, Lindborg, 2006, Brethouwer et al., 2007]. Gravity waves are not directly forced. Time dependence of the forcing follows an AR(1) red noise process with a set decorrelation time scale τ [Waite, 2017],

$$G(\vec{k}, t_n) = \tilde{\alpha} G(\vec{k}, t_{n-1}) + \tilde{\beta} g(\vec{k}, n), \tag{2.19}$$

for a random complex number $g(\vec{k}, n)$. The random number's real and imaginary parts follow a Gaussian distribution with a mean of 0 and variance of 1. The coefficients in equation (2.19) satisfy

$$\tilde{\alpha} = \exp(-\Delta t/\tau), \tag{2.20}$$

$$\tilde{\beta}^2 = 1 - \tilde{\alpha}^2. \tag{2.21}$$

A specified forcing amplitude multiplies $G(\vec{k}, t_n)$ and is applied to modes in the spherical shell $k \in [3, 5]$, with the decorrelation time scale set to 10 time steps. The simulations are initialized with a prescribed kinetic and potential energy at a chosen wavenumber $k = 3$. Damping is applied to the $k_h = 0$ modes to prevent the accumulation of energy in vertically sheared horizontal flow [Smith and Waleffe, 2002]. More details on the code used for these simulations can be found in past studies [Waite, 2011, 2017].

The first set of simulations has a fixed buoyancy frequency N, and separate trials for each Prandtl number. This approach was repeated for a total of 4 stratification strengths

and 5 Prandtl numbers, resulting in 20 simulations at the same resolution with $Pr = 0.7$, 1, 2, 4, and 8 (runs with labels 0, 1, 2, 3, and 4 respectively) and $N = 0.075$, 0.15, 0.3, and 0.6 (runs with labels A, B, C, and D respectively). The values for N were chosen to give a range of Fr_h, and values for Re_b of $O(1)$ and larger. The most strongly stratified cases have $Fr_h \approx 0.01$; for a lab experiment setup where $U = 10^{-2}$ ms^{-1} and $L_h = 2$ m, this Fr_h corresponds to a 2.5% change in density over a depth of 1 meter (or 1.25% if $L_v = 0.5$ m in the setup, for example). For every run, the kinematic viscosity is set to be the same: $\nu = 1.2 \times 10^{-5}$. The resolution $n = 1536$ ensures that the Kolmogorov scale is well resolved ($k_{max}/k_d \approx 3$), and that k_θ is resolved ($k_{max}/k_\theta > 1$) except for when $Pr = 8$. The simulations with $Pr = 8$ are slightly underresolved compared to the others, with $k_{max}/k_\theta \approx 0.7$, but these results are still included for comparison and may still be considered DNS since $k_{max}/k_\theta \sim 1$ [Moin and Mahesh, 1998]. In addition to studying dependence on Pr, these parameter values explore both regimes of strongly stratified turbulence, $Re_b < 1$ and $Re_b > 1$.

2.3 Physical space field derivatives, probability density functions, and statistics

For the investigation into local isotropy and comparison with de Bruyn Kops [2015], derivatives of the temperature and velocity component fields are calculated in MATLAB, making use of the Fourier transform and its inverse, `fftn`, and `ifftn`. For each simulation, derivatives in the x-, y-, and z-direction are computed for θ and for each component of $\vec{u} = (u_1, u_2, u_3)$. The velocity component derivative fields are denoted $u_{i,j}$ for the derivative with respect to j of the ith velocity component ($x = 1$, $y = 2$, and $z = 3$).

Probability density functions (p.d.f.s) of the temperature and velocity component fields are approximated and plotted using MATLAB's `ksdensity` instead of `histogram`. The result of this is a smoother line plot than if `histogram` were used. Due to the lower resolution in these simulations versus the ones in de Bruyn Kops [2015], p.d.f.s that were generated from `histogram` were fairly rough and difficult to compare.

The variance σ^2, skewness S, and kurtosis K of the derivative fields are calculated with built-in MATLAB functions `var`, `skewness`, and `kurtosis`. These statistical moments, or statistics, are often used in studies of turbulent flows and their use is discussed in introductory fluid mechanics and turbulence textbooks, e.g. Chapter 6 in Tennekes and Lumley [1972], Chapters 7 and 13 in Wyngaard [2010], Chapter 12 in [Kundu et al., 2012], and Chapter 5 in Davidson [2015]. The variance quantifies how far spread out the

distribution is from its mean (or average) value. The skewness is a measure of symmetry in the distribution about its mean. If the distribution tends to have more frequent instances of values less than the mean, S is negative. The kurtosis, or flatness factor, is a measure of how outlier-prone a distribution is, where $K = 3$ for a Gaussian distribution. These are calculated in MATLAB as

$$\sigma^2 = \frac{1}{n-1}\sum_{i=1}^{n}(x_i - \overline{x})^2, \tag{2.22}$$

$$S = \frac{\frac{1}{n}\sum_{i=1}^{n}(x_i - \overline{x})^3}{\left(\frac{1}{n}\sum_{i=1}^{n}(x_i - \overline{x})^2\right)^{3/2}}, \tag{2.23}$$

$$K = \frac{\frac{1}{n}\sum_{i=1}^{n}(x_i - \overline{x})^4}{\left(\frac{1}{n}\sum_{i=1}^{n}(x_i - \overline{x})^2\right)^{2}}, \tag{2.24}$$

for a set of data $\vec{x} = \{x_i\}$ with n data points (which is 1536^3 with our resolution) and a mean of $\overline{x}$ (which is 0 in our analysis).

The velocity and temperature fields in de Bruyn Kops [2015] were analyzed for their isotropy by identifying distinguishable groups in their statistics. In their isotropic benchmark case, velocity statistics markedly fell into either the longitudinal or transverse group. For the velocity, the longitudinal derivatives were $u_{1,1}$, $u_{2,2}$, and $u_{3,3}$, and the transverse derivatives were the remaining $u_{1,2}$, $u_{1,3}$, $u_{2,1}$, $u_{2,3}$, $u_{3,1}$, and $u_{3,2}$. Temperature derivatives were considered horizontal ($\theta_{,1}$ and $\theta_{,2}$) or vertical ($\theta_{,3}$). The stratified simulations, like ours, were axisymmetric and homogeneous. By axisymmetric it is meant that the statistics are independent of direction on a horizontal plane (e.g. derivatives in the x- and y-directions would have the same statistics). Due to axisymmetry, the velocity derivatives would have 5 statistically independent derivatives corresponding to the groups

$$u_{1,1}, u_{2,2}; \quad u_{1,2}, u_{2,1}; \quad u_{3,3}; \quad u_{1,3}, u_{2,3}; \quad u_{3,1}, u_{3,2}.$$

The first two groups come from interchangeability of 1 and 2 in the longitudinal and transverse derivatives respectively. Similarly, the fourth group pairs the z-derivatives of the x- and y-components together, and the fifth group pairs the x- and y-derivatives of the z-components together. However, their low Re_b (strongly stratified) case suggested 3 distinct groups

$$u_{1,1}, u_{2,2}, u_{3,3}; \quad u_{1,2}, u_{2,1}, u_{3,1}, u_{3,2}; \quad u_{1,3}, u_{2,3}.$$

Higher Re_b (weaker stratification) suggested 2 groups, expected of the turbulently-coupled-layers regime being more similar to the isotropic case.

To obtain ensemble-averaged data, time averaging of the p.d.f.s is done over the second half of simulation time, roughly corresponding to the same simulation time interval mentioned in 2.2, which include the last 5 output NetCDF files in each simulation (the simulations analyzed in comparison with de Bruyn Kops [2015] used 9 output times for physical space fields).

For each of u_1, u_2, u_3, and θ, the computations for every simulation follow:

1. Read the last 5 NetCDF output files (`ncread`) and compute the $(\cdot)_{,1}$, $(\cdot)_{,2}$, and $(\cdot)_{,3}$ derivatives, resulting in 5 sets of 3 derivative directions,
2. For each derivative direction, combine the data from all 5 output times into a single array (e.g. create `u31` that will include $u_{3,1}$ data from the 5 NetCDF files),
3. Compute histogram data with `ksdensity`, then time-average by scaling frequency data by 1/5,
4. Plot p.d.f.s and compute statistics of the now time-averaged data.

Chapter 3

Results

In Chapter 3 we analyze kinetic and potential energy spectra, spectral budget terms, and physical space fields of the simulations. We start with $Pr = 1$, first focusing on the $N = 0.3$ case (Sec. 3.1.1), then we look at the effect of varying N for the $Pr = 1$ cases (Sec. 3.1.2). Next, in Sec. 3.2 we analyze the spectra and snapshots for Pr-dependence. Finally, in Sec. 3.3, p.d.f.s and statistics for each simulation are studied to determine how Pr affects isotropy in the velocity component and temperature fields.

3.1 Overview of $Pr = 1$ cases

3.1.1 Overview of the $N = 0.3$, $Pr = 1$ case

We start with an overview of the $Pr = 1$ case with intermediate stratification $N = 0.3$ (run C1). Time series of kinetic and potential energy and dissipation are plotted in Fig. 3.1(a,c). The energy and dissipation rates increase for the first 200 time units until the flow develops into statistically stationary turbulence, after which these quantities equilibrate. The energy and dissipation plots are fairly steady for $t \in [300, 500]$, which is chosen as the time averaging interval. Stationarity at these times is observed for all the simulations, so the same time averaging interval is used for all cases.

Horizontal and vertical wavenumber spectra are plotted in Fig. 3.1(b,d) (the full wavenumber energy spectra are omitted as they closely resemble the vertical spectra). Spikes in the kinetic energy spectra for small wavenumbers are a consequence of the large-scale forcing

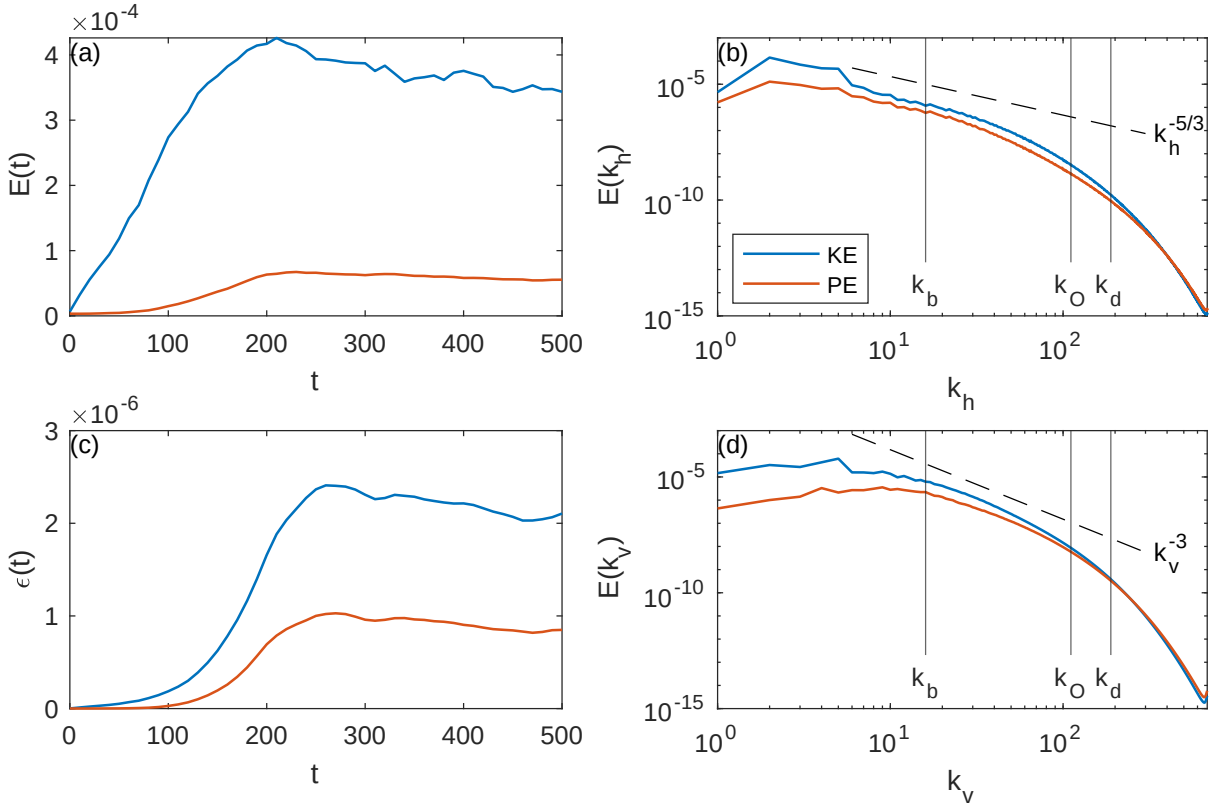

Figure 3.1: Energy spectra and time series for run C1: $Pr = 1$, $N = 0.3$. Left column: time series of (a) kinetic and potential energy and (c) energy dissipation. Right column: kinetic and potential energy spectra in terms of (b) horizontal and (d) vertical wavenumber. Characteristic wavenumbers k_b, k_O, and k_d are denoted with vertical solid lines, and reference slopes are given by dashed lines. Note that k_θ is coincident with k_d for $Pr = 1$.

for $k \in [3, 5]$. For $Pr = 1$, k_d and k_θ (label omitted) are coincident. Beyond the forcing interval, the horizontal spectra are close to the expected $k_h^{-5/3}$ scaling law for approximately one decade [Lindborg, 2006]. The vertical kinetic energy spectrum is flat out to k_b, while the potential energy spectrum is peaked at k_b. Beyond k_b, the vertical spectra steepens to approximately k_v^{-3}. Due to the modest $Re_b = 2.03$ in this case, there is only a small separation between the Ozmidov and dissipation scales. Since $Pr = 1$, the kinetic and potential energy are expected to behave similarly at very small scales as both momentum- and buoyancy-diffusive scales are equivalent; indeed, in the dissipation range beyond k_d (or k_θ), the spectra are nearly the same.

Figure 3.2 shows vertical and horizontal slices of horizontal velocity and vorticity at the end of the simulation. With $Re_b = 2.03$ and $Fr_h = 0.019$, run C1 is in the strongly stratified and slightly viscous regime where the flow is arranged into layers of pancake eddies. This run is only slightly past the $Re_b = 1$ transition from viscously to turbulently coupled layers. In Fig. 3.2(a,b), the layerwise arrangement and intermittent small-scale Kelvin-Helmholtz (KH) instabilities can be seen clearly in the vertical slices of the velocity and y-component vorticity fields. The buoyancy wavenumber $k_b = 16$ for run C1 is approximately the number of layers in the flow. The horizontal slices of velocity and z-component vorticity fields in Fig. 3.2(c,d) clearly show the signature of the large-scale vortical forcing. In addition, small horizontal scales associated with KH billows are visible in Fig. 3.2(d).

The temperature fluctuation dissipation field (equation (1.14)) is shown in Fig. 3.3. Run C1 has few regions that are highly θ-dissipative, and in Fig. 3.3(a) the θ-dissipative regions resemble small quasi-horizontal features in contrast with the intermittent worms expected in unstratified homogeneous 3D turbulence [Burgers, 1948, Siggia, 1981, Ishihara et al., 2013]. These dissipative regions also appear to be arranged in horizontal layers (Fig. 3.3(b)) as in the vertical slices of u and ω_y in Fig. 3.2(a,b).

We now consider the spectral budget for run C1. The spectra of T_K, T_P, and B from the energy budget (2.5)-(2.6) are plotted for run C1 in Fig. 3.4(a,b). Since these spectra are obtained by time averaging over the stationary interval, the dissipation spectra can be obtained as a residual: e.g. $D_K(k) \approx T_K(k) + B(k)$ outside the forcing interval. The horizontal and vertical spectral budgets are similar at large scales; the shape of the spectra at small wavenumbers is primarily influenced by the large-scale forcing. In the forcing interval, there is substantial transfer of the injected kinetic energy out of the forced wavenumbers, as indicated by large negative spikes in $T_K(k_h)$ and $T_K(k_v)$. The potential energy budget terms $T_P(k_h)$, $T_P(k_v)$, $B(k_h)$ and $B(k_v)$ are very small and negative in this range, indicating that, while there is no direct forcing of potential energy, there is some conversion of the remaining injected kinetic energy to potential energy.

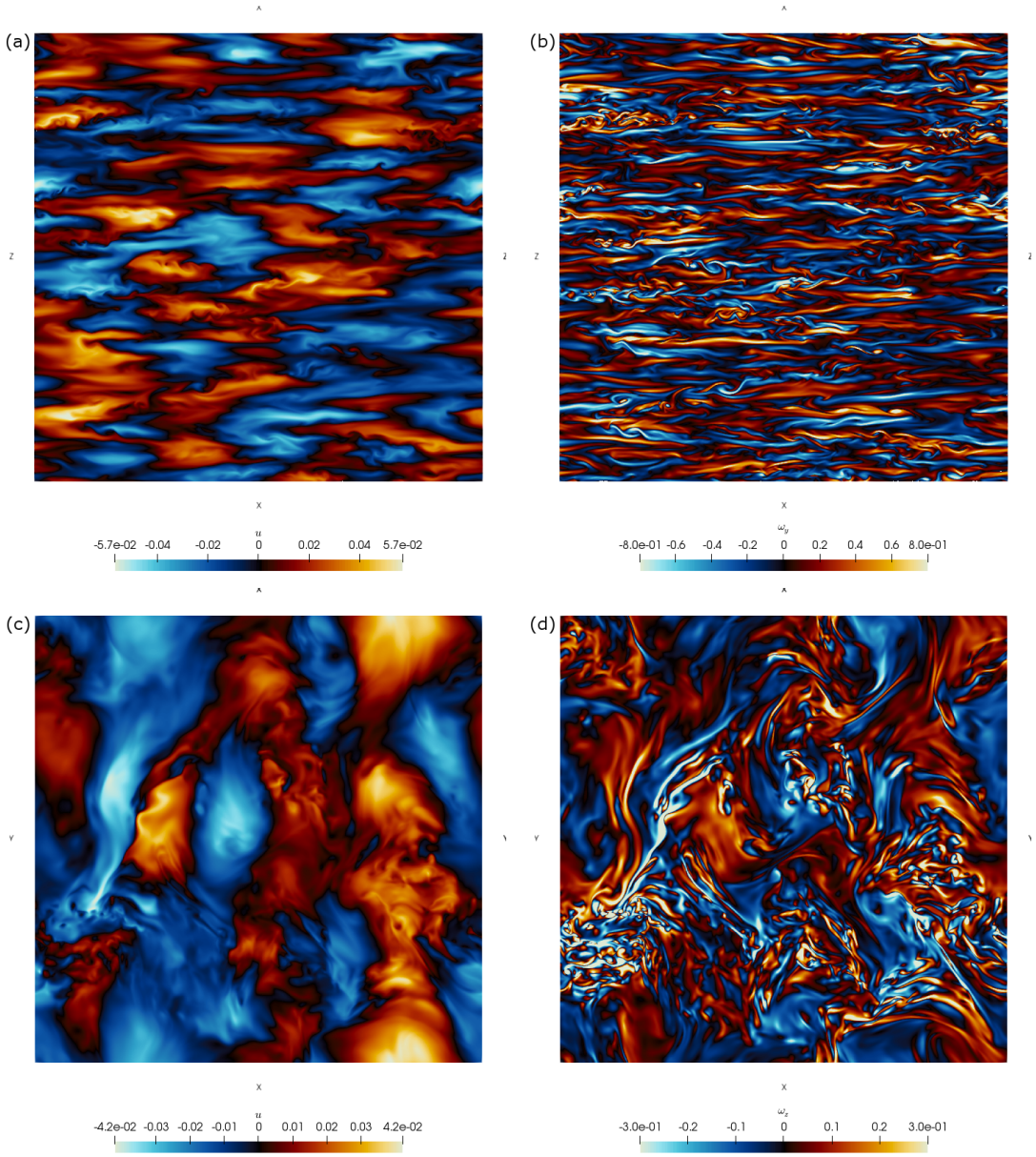

Figure 3.2: Top row: vertical slices (x, z) at $y = 0$ of (a) x-component velocity u and (b) y-component vorticity ω_y. Bottom row: horizontal slices (x, y) at $z = 0$ of (c) x-component velocity u and (d) z-component vorticity ω_z. All fields are computed at the end of run C1.

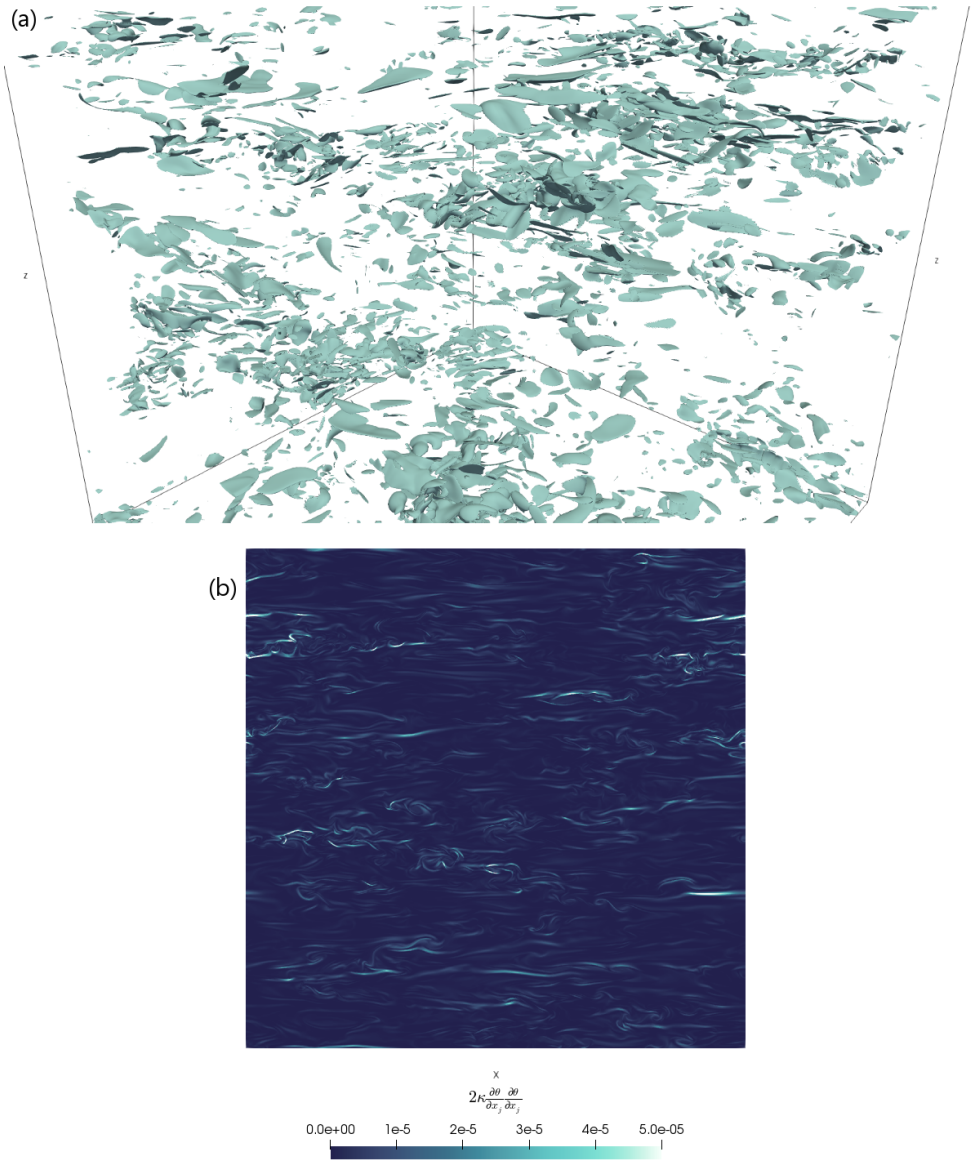

Figure 3.3: Temperature fluctuation dissipation field, $2\kappa\frac{\partial\theta}{\partial x_j}\frac{\partial\theta}{\partial x_j}$: (a) isosurfaces of 5% of the maximum value, (b) vertical slice (x, z) at $y = 0$. All fields are computed at the end of run C1.

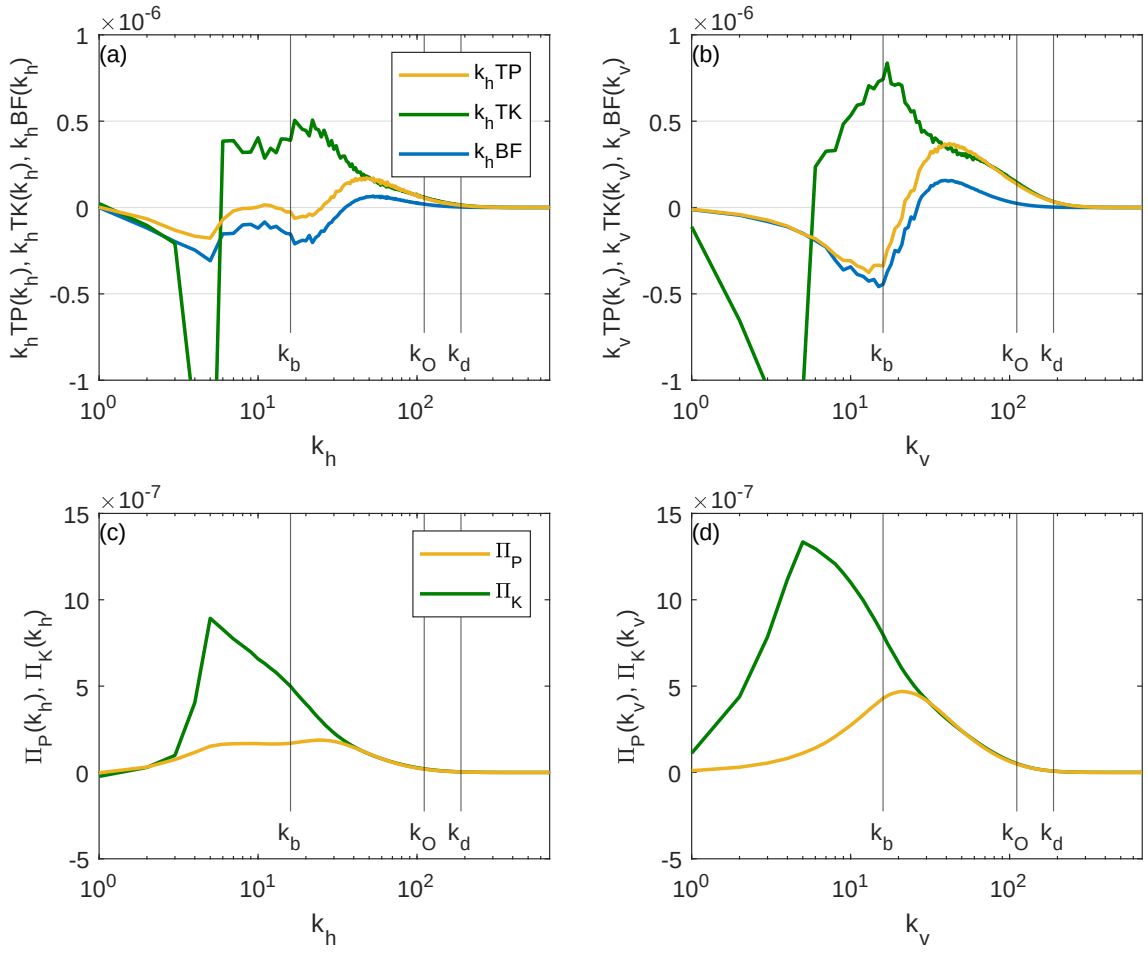

Figure 3.4: (a,b): Spectra for kinetic and potential energy transfer terms and buoyancy flux for run C1. Spectra are multiplied by wavenumber to preserve area under the curve for linear-log axes. (c,d): Spectral energy fluxes plotted for run C1.

In the horizontal spectral budget, downscale of the forcing interval, $T_K(k_h)$ is positive and has a small peak at k_b. Some of the kinetic energy deposited at these wavenumbers is converted to potential energy, as indicated by the negative buoyancy flux in this range. Indeed, between the forcing interval and k_b, $T_P(k_h)$ and $B(k_h)$, both of which are negative, increase to near zero. Comparing the energy budget terms in this range reveals that much of the energy going into these horizontal scales is lost to dissipation: dissipation at large and intermediate horizontal scales can occur at large Re through the vertical part of the dissipation term, which is restricted to small vertical scales but not necessarily small horizontal scales, since Re_b is not very large in this case. Dissipation at small wavenumbers disrupts the formation of a distinguishable true inertial subrange, which will be apparent in the spectral energy flux.

At k_b, $T_P(k_h)$ and $B(k_h)$ exhibit negative peaks coinciding with $T_K(k_h)$'s positive peak, but are much smaller in comparison. Overturning from the formation, instability, and breakdown of horizontal layers characteristically occurs at the buoyancy scale, so some conversion of kinetic to potential energy is expected at k_b, as seen in Holloway [1988], Waite [2011, 2014].

The vertical spectral budget shows different behaviour between the forcing interval and the buoyancy scale. At k_b, $T_K(k_v)$ has a prominent positive peak while $T_P(k_v)$ and $B(k_v)$ have negative peaks, and they are all comparable in magnitude indicating a smaller energy loss to dissipation than in the horizontal spectral budget. It is clear that in the vertical spectral budget, the overturning occurring at k_b is far more efficient at converting kinetic energy to potential energy than the horizontal.

Downscale of k_b and into the dissipation range, the horizontal and vertical spectral budgets behave similarly again. Between k_b and k_O, all of $T_P(k_h)$, $T_P(k_v)$, $B(k_h)$ and $B(k_v)$ increase to positive spectral peaks. At length scales below the buoyancy scale, buoyancy-driven processes dominate and large amounts of potential energy are expended to restratify the flow. Past k_O, viscous dissipation and buoyancy diffusion take over as $T_K(k_h)$, $T_K(k_v)$, $T_P(k_h)$, $T_P(k_v)$, $B(k_h)$, and $B(k_v)$ decrease to zero.

The spectral energy fluxes Π_K and Π_P are shown in Fig. 3.4(c,d). While the fluxes are positive beyond the forcing scale, consistent with a downscale transfer of kinetic and potential energy, they do not exhibit discernable wavenumber ranges where downscale energy flux is constant. However, since $T_P(k_h)$ is almost zero for a short wavenumber interval, there is more of a range of constant flux in potential than kinetic energy. The absence of a long inertial subrange is not unexpected, given the modest Re and Re_b of this case [Brethouwer et al., 2007]. Beyond the forcing interval, $\Pi_K(k_h)$ and $\Pi_K(k_v)$ exhibit a large positive peak at larger wavenumbers. Dissipation at these large scales reduces

the available energy for downscale transfer, inhibiting the development of a true inertial subrange.

The spectral fluxes for potential energy are smaller than the kinetic spectral fluxes at small horizontal and vertical wavenumbers, as the extreme negative spikes in $T_K(k_h)$ and $T_K(k_v)$ are directly caused by the large-scale forcing of kinetic energy. However, beyond the buoyancy scale, the kinetic and potential fluxes converge. The horizontal spectral fluxes in run C1 are small compared to the vertical spectral fluxes; this tends to depend on N, and will be further discussed in §3.2.3.

3.1.2 N-dependence for $Pr = 1$

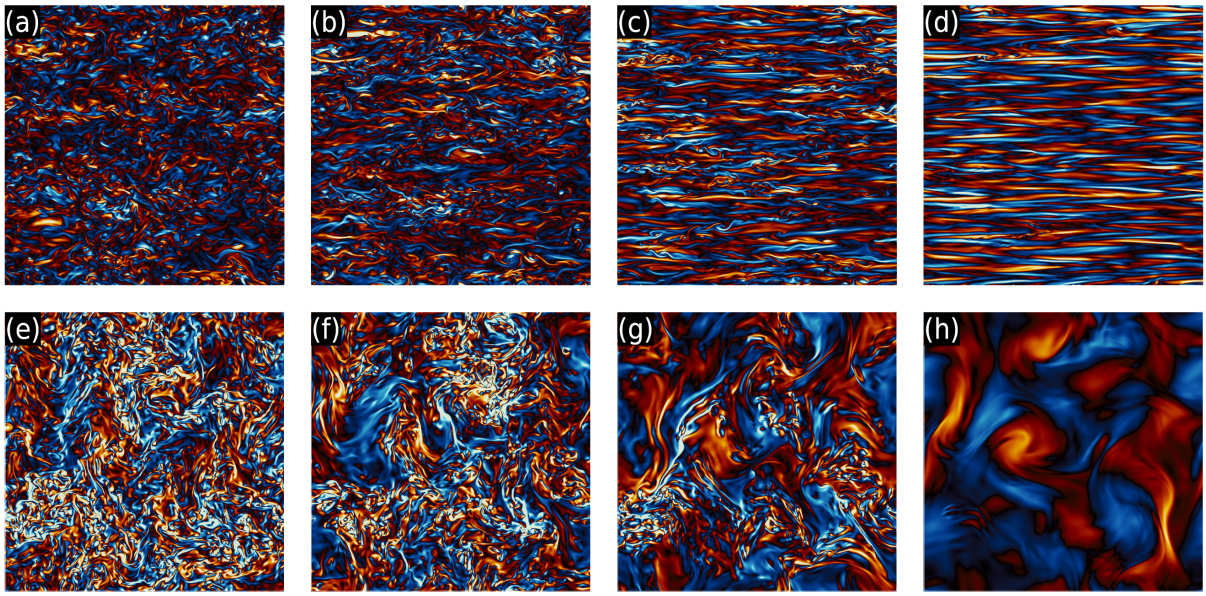

Figure 3.5: Top row: vertical slices (x, z) at $y = 0$ of y-component vorticity. Bottom row: horizontal slices (x, y) at $z = 0$ of z-component vorticity. $Pr = 1$ for (a,e) $N = 0.075$, (b,f) $N = 0.15$, (c,g) $N = 0.3$, and (d,h) $N = 0.6$. The same colourmap is used as in Fig. 3.2 with the range modified for visibility across N. The colourmap range shared by the vertical slices is different from the range shared by the horizontal slices.

With fixed $Pr = 1$, increasing N from 0.075 to 0.6 decreases Re_b from 28.7 to 0.567, and Fr_h from 0.0947 to 0.00935. Through the vertical slices in panels (a)-(d) of Figs. 3.5 and 3.6, we observe the transition in regimes from nearly isotropic small and intermediate scales

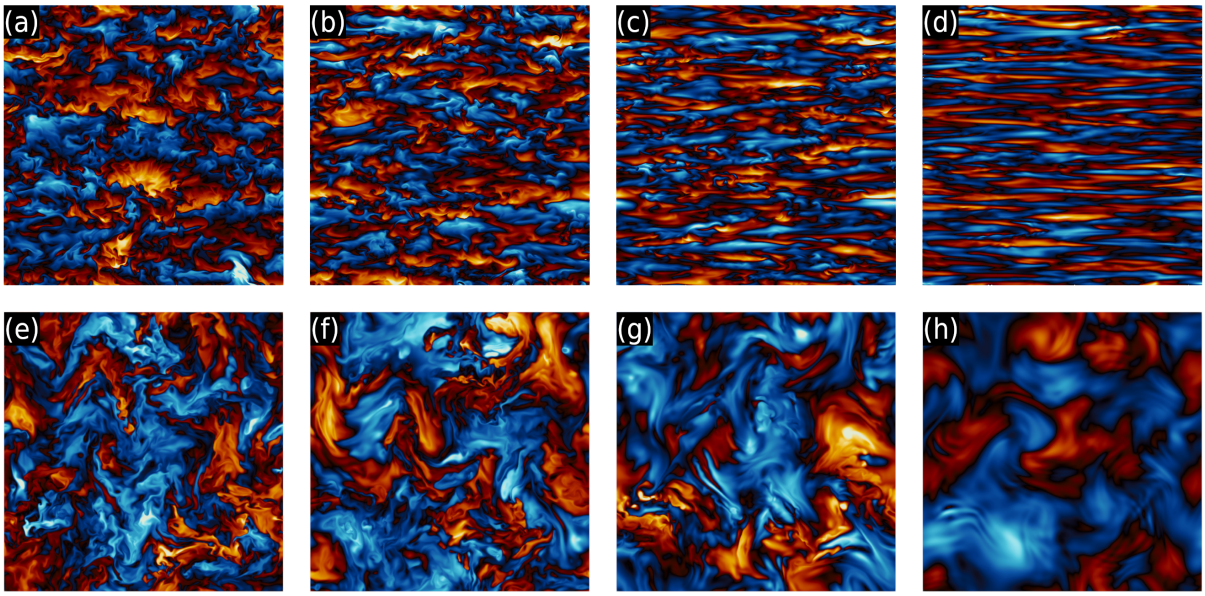

Figure 3.6: Top row: vertical slices (x, z) at $y = 0$ of θ. Bottom row: horizontal slices (x, y) at $z = 0$ of θ. $Pr = 1$ for (a,e) $N = 0.075$, (b,f) $N = 0.15$, (c,g) $N = 0.3$, and (d,h) $N = 0.6$. The same colourmap is used as in Fig. 3.2 with the range modified for visibility across N. The colourmap range shared by the vertical slices is different from the range shared by the horizontal slices.

to horizontally-layered flow in the vorticity and temperature fluctuation fields. Obvious layers are not visible in the vorticity field at the weakest stratification $N = 0.075$; the vertical temperature field slice in Fig. 3.6(a) better shows the slight anisotropy at $Re_b = 28.7$. At intermediate stratifications $N = 0.15$ and 0.3, KH instabilities are visible within recognizable horizontal layers in both the vorticity and temperature fields. Increasing N reduces the thickness of these layers, corresponding to an increase in k_b. For the strongest stratification $N = 0.6$, overturning is restricted to very small vertical scales and only a few instabilities are visible in Figs. 3.5,3.6(d).

The horizontal slices in panels (e)-(h) of Figs. 3.5 and 3.6 show the loss of small scale features, as the small scales become less turbulent with greater N. This loss of small features can be attributed to k_O growing from 15 to 297 between $N = 0.075$ and 0.6 while k_d is only slightly increased. At lower N, the flow resembles small scale isotropic turbulence for a wider wavenumber range $k \in [k_O, k_d]$, so the loss of small-scale features at $N = 0.6$ is in line with greater anisotropy. At $N = 0.6$, signatures of KH billows are still visible in the horizontal slices Figs. 3.5,3.6(h). These panels also exhibit the least extreme values in temperature and vorticity: as the horizontal layers are reduced to vertical scales near k_d (and k_θ in the case of $Pr = 1$), fluctuations in these fields are eliminated by viscous dissipation and buoyancy diffusivity.

The kinetic and potential energy spectra for $Pr = 1$ at each N are plotted in Fig. 3.7 in terms of horizontal and vertical wavenumber. For the horizontal kinetic energy spectra in Fig. 3.7(a), the $N = 0.075$, 0.15, and 0.3 cases are very similar. Slightly more kinetic energy is found at large scales for larger N, and these cases show agreement with the $k_h^{-5/3}$ scaling law for about a decade after the forcing interval. The vertical kinetic energy spectra in Fig. 3.7(b) are also affected by N. As k_b increases with N, these spectra are relatively flat for a longer range of small wavenumbers, but eventually converge at $k_v \approx 100$. Limited agreement with k_v^{-3} scaling is observed at the three lowest stratifications.

The horizontal potential energy spectra for $N = 0.075$, 0.15, and 0.3 follow the same patterns as the kinetic energy, but with marginally more N-dependence at intermediate and large k_h. Downscale of k_b, the spectra steepen more for larger N but eventually converge far into the dissipation range. More potential energy is found at intermediate to large k_h at weaker stratification which is consistent with more small scale overturning in the temperature field. The vertical potential energy spectra peak at their respective k_b, and exhibit similar dependence on N as in the vertical kinetic energy spectra.

In all panels, the $N = 0.6$ spectra have a distinct shape compared to the lower three stratifications. Since $Re_b = 0.6 < 1$, the cascade to small horizontal scales is suppressed and there is a consequent steepening of the horizontal spectra (e.g. [Brethouwer et al., 2007,

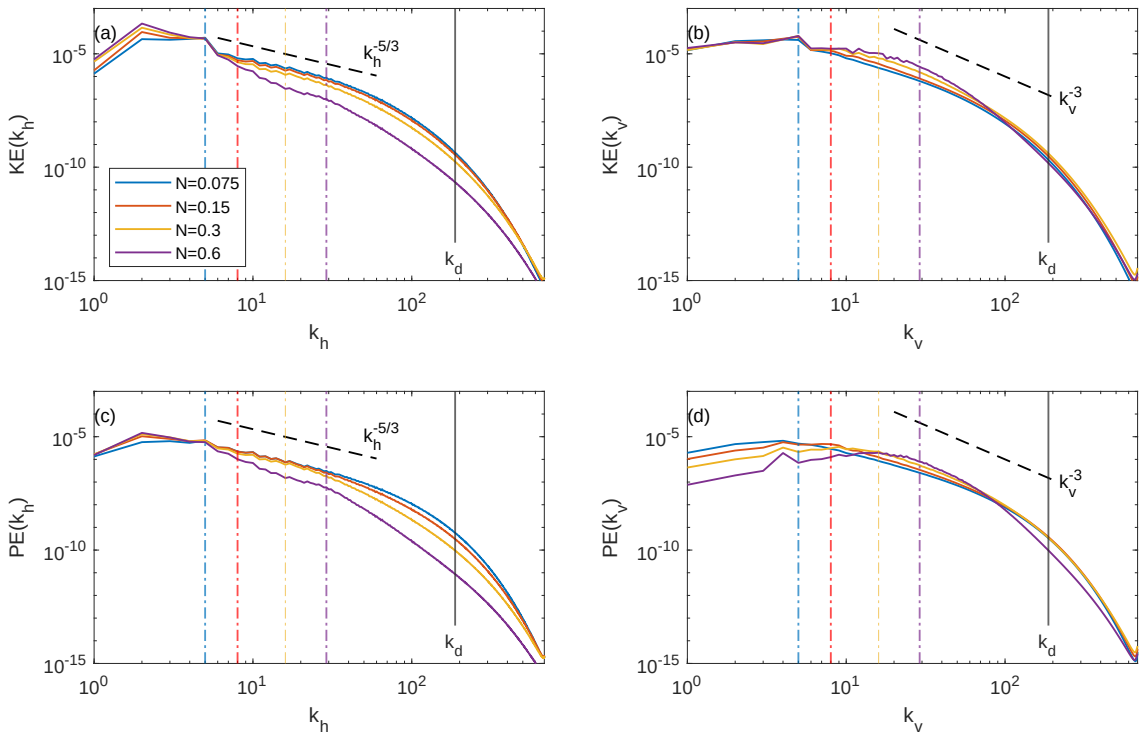

Figure 3.7: Energy spectra in terms of horizontal and vertical wavenumbers for $Pr = 1$ at different N. Black dashed lines are $k_h^{-5/3}$ and k_v^{-3} reference lines. Vertical dash-dotted lines are buoyancy scales corresponding to N colours. The average k_d and k_θ are the same for $Pr = 1$.

Waite, 2014]). The steepening of the $N = 0.6$ horizontal spectra at small wavenumbers is severe enough that there is little $k_h^{-5/3}$ scaling law agreement just downscale of the forcing. Similarly, the steepening from k_b onwards causes the $N = 0.6$ vertical spectra to deviate from k_v^{-3} scaling. Except in Fig. 3.7(b), the $N = 0.6$ case does not converge to the other three cases until the end of the wavenumber range. Strong stratification will restrict vertical advection, which greatly reduces the potential energy found at small vertical length scales.

3.2 Pr-dependence

3.2.1 Energy spectra

We now examine the effects of varying Pr in fixed-N groups, starting with the kinetic and potential energy spectra. For all values of N, the horizontal and vertical kinetic energy spectra, shown in Fig. 3.8, do not appear to be significantly affected by Pr. As in Fig. 3.1, spikes at small wavenumbers are from the large-scale forcing, and the vertical spectra are flat until k_b. For $N = 0.075$, 0.15, and 0.3, the horizontal spectra follow the $k_h^{-5/3}$ scaling law just after the forcing interval for about one decade as in run C1 (see Table 3.1). The $N = 0.6$ spectra are steeper than those at lower N, with a more pronounced bump at k_b [Waite, 2014]. Similarly, the k_v^{-3} scaling law for vertical wavenumber spectra is observed for about one decade for all groups except $N = 0.6$. Beyond these short scaling law intervals, both the horizontal and vertical spectra shallow slightly when Pr is increased (Table 3.1). Larger-Pr simulations contain more kinetic energy at small scales since buoyancy-induced velocity fluctuations can persist as k_θ increases. As a result of the spectra shallowing, the $k_h^{-5/3}$ and k_v^{-3} scaling laws extend to slightly smaller scales.

As stratification increases, the dependence on Pr extends to smaller wavenumbers. For example, the horizontal kinetic energy spectra for different Pr start to diverge at $k_h \approx 50$ for $N = 0.075$ and $k_h \approx 20$ for $N = 0.3$ in Figs. 3.8(a) and 3.8(e) respectively. Only for the horizontal spectra with $N = 0.6$ (Fig. 3.8(g)) do the spectra for each Pr separate shortly after the forcing interval, and at a wavenumber smaller than k_b.

The potential energy spectra in Fig. 3.9 show similar but more pronounced changes as Pr is varied. Both horizontal and vertical spectra exhibit the same shallowing with increased Pr at large wavenumbers as in the kinetic energy spectra (Table 3.1). In the horizontal spectra, the shallowing that results from increasing Pr again lengthens the wavenumber range for which there is agreement with $k_h^{-5/3}$ scaling. Increasing N increases the average k_b, where peaks in vertical spectra are observed. As in run C1, this differs

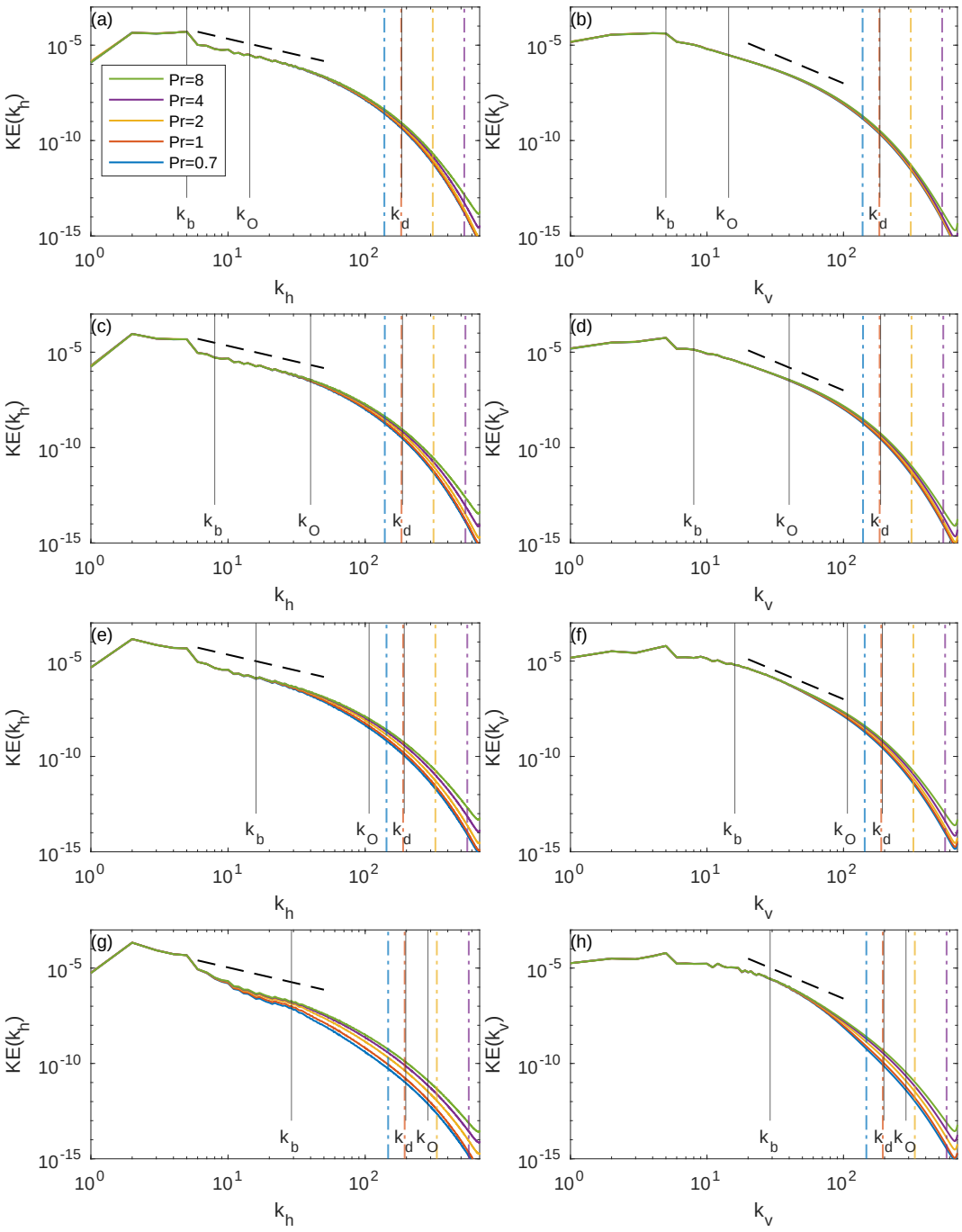

Figure 3.8: Kinetic energy spectra in terms of horizontal and vertical wavenumbers. From top to bottom the rows are $N = 0.075, 0.15, 0.3, 0.6$. Black dashed lines are $k_h^{-5/3}$ and k_v^{-3} reference lines. Vertical dash-dotted lines are k_θ corresponding to Pr colours.

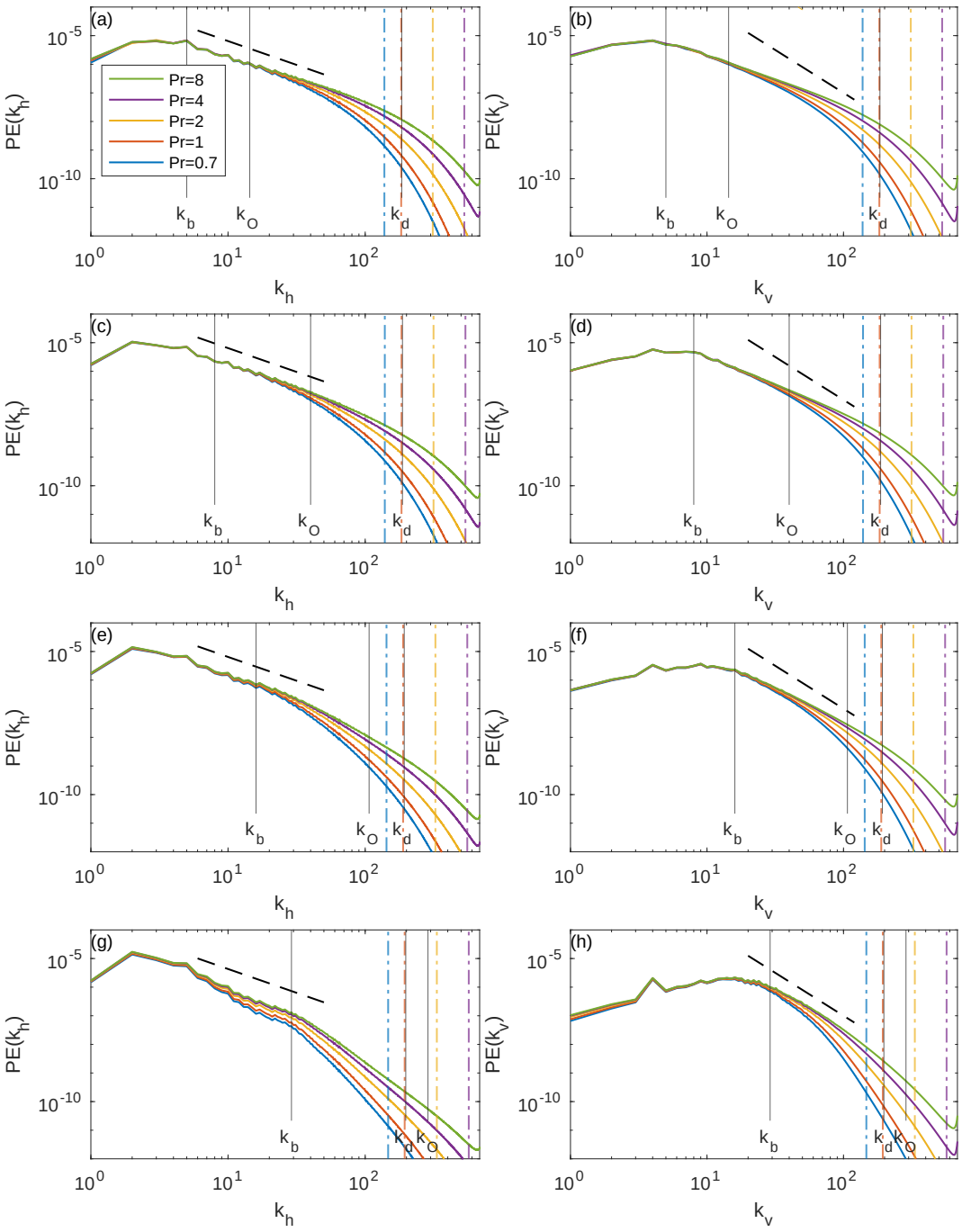

Figure 3.9: Potential energy spectra in terms of horizontal and vertical wavenumbers. From top to bottom the rows are $N = 0.075, 0.15, 0.3, 0.6$. Black dashed lines are $k_h^{-5/3}$ and k_v^{-3} reference lines. Vertical dash-dotted lines are k_θ corresponding to Pr colours.

Run	N	Pr	$KE(k_h)$	$KE(k_v)$	$PE(k_h)$	$PE(k_v)$
A0	0.075	0.7	-2.04	-2.43	-1.98	-2.21
A1	0.075	1	-2.01	-2.41	-1.84	-2.07
A2	0.075	2	-1.97	-2.39	-1.67	-1.90
A3	0.075	4	-1.95	-2.36	-1.55	-1.77
A4	0.075	8	-1.93	-2.35	-1.47	-1.69
B0	0.15	0.7	-2.09	-2.79	-2.20	-2.59
B1	0.15	1	-2.04	-2.76	-2.07	-2.43
B2	0.15	2	-1.96	-2.70	-1.87	-2.20
B3	0.15	4	-1.92	-2.66	-1.75	-2.07
B4	0.15	8	-1.89	-2.64	-1.67	-1.98
C0	0.3	0.7	-2.35	-4.07	-2.51	-3.91
C1	0.3	1	-2.26	-3.97	-2.35	-3.53
C2	0.3	2	-2.13	-3.82	-2.13	-3.00
C3	0.3	4	-2.05	-3.70	-1.98	-2.67
C4	0.3	8	-2.00	-3.62	-1.89	-2.47
D0	0.6	0.7	-2.92	-5.85	-2.46	-5.86
D1	0.6	1	-2.76	-5.63	-2.31	-5.26
D2	0.6	2	-2.55	-5.26	-2.13	-4.33
D3	0.6	4	-2.43	-4.97	-2.02	-3.69
D4	0.6	8	-2.38	-4.77	-1.96	-3.27

Table 3.1: Slopes from linear regression analysis of kinetic and potential energy spectra in Figs. 3.8 and 3.9. For horizontal spectra, the linear regression is performed over $k_h \in [6, 60]$ except for $N = 0.6$, where $k_h \in [6, 29]$ is used. For vertical spectra, the wavenumber interval is one decade starting at k_b; i.e. $k_v \in [6, 60], [8, 80], [16, 160]$ for $N = 0.075, 0.15, 0.3$ respectively. The vertical spectra for $N = 0.6$ uses $k_v \in [29, 200]$ since the average $k_d \approx 198$.

from the kinetic energy spectra which are flat until k_b. In the vertical spectra for $N = 0.075$, 0.15, and 0.3, the shallowing from larger Pr causes the spectra to stray from the k_v^{-3} scaling law downscale of k_b.

A similar trend as the kinetic energy spectra is observed for the $N = 0.6$ potential energy spectra (Fig. 3.9(g,h)): here, both the horizontal and vertical spectra visibly separate just after the forcing interval and before k_b. The separation occurs at a noticeably smaller wavenumber for the horizontal spectra than the vertical, as in the kinetic energy case. All simulations with $N = 0.6$ have $Re_b < 1$; horizontal scales between the forcing interval and the buoyancy scale would be sensitive to Pr because of the instabilities that form between the layers of quasi-horizontal vortices. Figure 3.9(g) for $N = 0.6$ also shows a break in the horizontal spectra at k_b, after which each curve steepens beyond $k_h^{-5/3}$.

For each increase in Pr, there appears to be less of a change in the shape of the spectra, and this behaviour is observed at all N. Excluding $Pr = 0.7$, each jump in Pr is from doubling the previous Pr, but the shallowing or separation between successive curves slightly decreases, as evident in Table 3.1. For instance, at the average $k_d = 193$ for $N = 0.3$, between $Pr = 1$ and $Pr = 2$ the horizontal kinetic energy increases by 67% compared to a 38% increase from $Pr = 4$ to $Pr = 8$. The vertical potential energy for the same N and k_d increases by 310% between $Pr = 1$ and $Pr = 2$ compared to a 76% increase from $Pr = 4$ to $Pr = 8$. Simulations where Pr is much greater than 8 may be expected to continue exhibiting less of a change in the potential energy spectra shape as Pr is increased. That is, the diminishing increase and shallowing of spectra at larger Pr may become so inappreciable that these higher-Pr spectra converge to a shape not vastly different from the $Pr = 8$ case. This convergence may hold as long as Pr is not extremely large: for very large $Pr \sim O(10^3)$ in decaying turbulence simulations, buoyant scalars have been shown to behave as passive scalars (i.e. potential energy spectra proportional to k^{-1}), and plateaus ($\propto k^0$) eventually develop in the potential energy spectra [Okino and Hanazaki, 2017].

3.2.2 Buoyancy flux

Buoyancy flux spectra are shown in Fig. 3.10 at different Pr in fixed-N groups as in §3.2.1 for the energy spectra. Overall, an increase in buoyancy flux is observed in all cases as Pr is increased. The increase in buoyancy flux is most significant at large horizontal and vertical wavenumbers, where restratification occurs, and is amplified at greater N. The one exception to this trend is for the strongest stratification (Fig. 3.10(g)), where the increased buoyancy flux is greatest at small horizontal and large vertical wavenumbers.

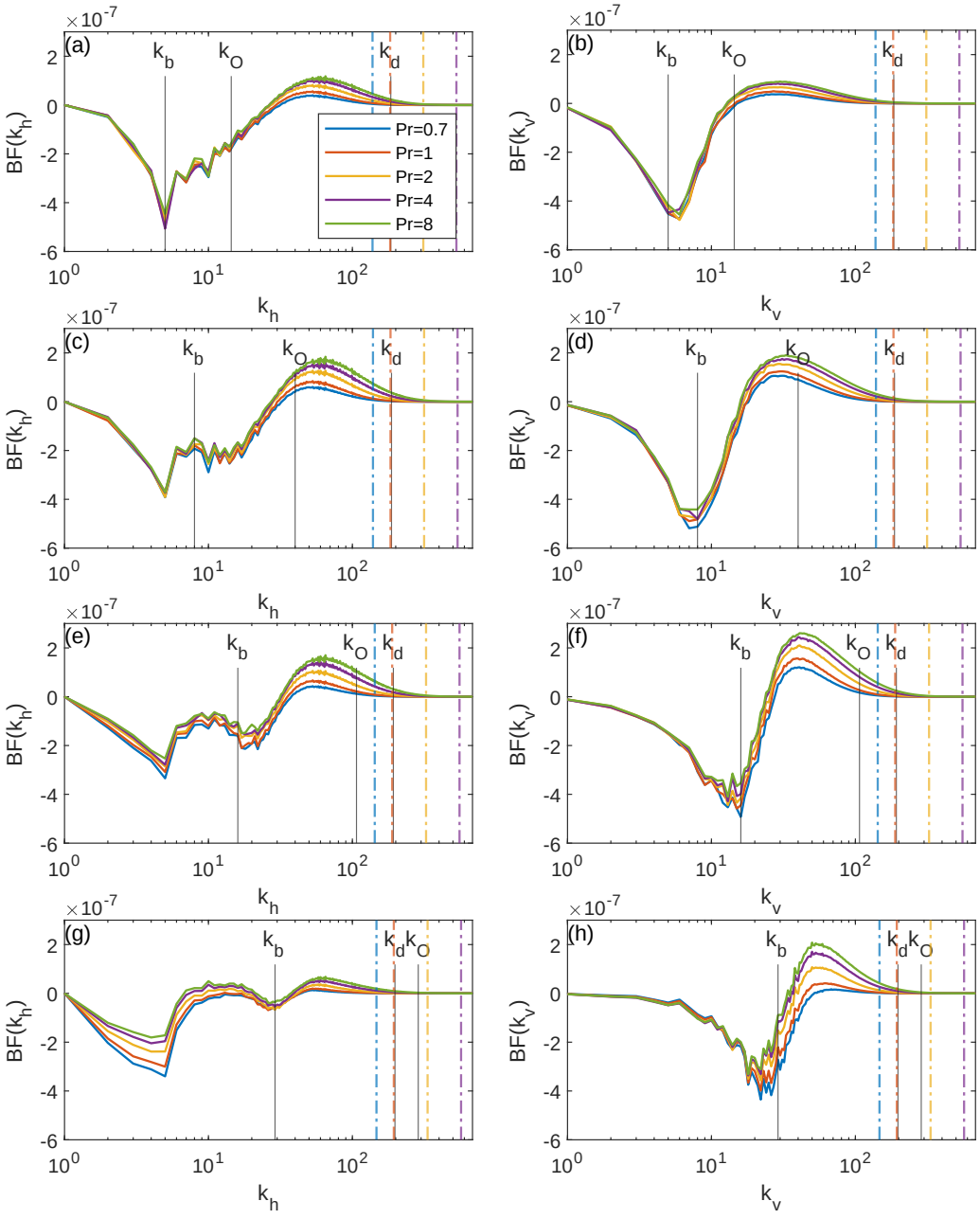

Figure 3.10: Buoyancy flux spectra multiplied by wavenumber to preserve area under the curve for linear-log axes. From top to bottom the rows are $N = 0.075$, 0.15, 0.3, and 0.6. Horizontal (left) and vertical (right) wavenumber spectra are shown. Vertical dash-dotted lines are k_θ corresponding to Pr colours.

Additionally, at $N = 0.6$, the horizontal buoyancy flux is positive for a short wavenumber range before k_b, as well as at larger (restratifying) wavenumbers, for $Pr = 2$, 4, and 8. It makes sense that a greater amount of potential energy is converted to kinetic energy as Pr is increased: there is more potential energy available at large wavenumbers for either nonlinear transfer or conversion to kinetic energy when buoyancy diffusivity is weakened (Fig. 3.9). Restratification is less suppressed for less intense turbulence [Holloway, 1988]; indeed, for these simulations, increasing Pr at a fixed N is associated with a decrease in Re.

The right column of Fig. 3.10 shows restratification to consistently take place at small vertical scales downscale of k_b. Due to the tendency towards isotropy at small scales, this positive spectral bump is also observed in the horizontal buoyancy flux spectra at a comparable k_h range, at least for $N = 0.075$, 0.15, and 0.3. The $N = 0.6$ case is different. All these simulations have $Re_b < 1$; as a result, there is no small-scale isotropy, and these small vertical scales are associated with large horizontal scales by viscously coupled layers. In this regime of stratified turbulence, it is reasonable that the buoyancy flux at large horizontal scales is heavily affected by Pr, since buoyancy diffusion at small vertical scales can characteristically occur between these layers. Fig. 3.10(g) also reveals that the Pr-dependence of buoyancy flux is sensitive enough at large horizontal scales to even decide the direction of kinetic-to-potential energy conversion. Buoyancy diffusion can become weak enough at a sufficiently large Pr so that at large horizontal scales, enough surplus potential energy may be made available for a positive buoyancy flux.

The dependence on Pr seems to be decreasing with increasing Pr, as seen in the energy spectra. For example, the separation between the buoyancy flux spectra in the $Pr = 4$ and $Pr = 8$ cases is noticeably smaller than for preceding Pr increments. This suggests convergence of the buoyancy flux spectra at large Pr (even moreso than for the energy spectra).

3.2.3 Spectral flux

The spectral energy fluxes Π_K and Π_P are shown in Figs. 3.11 and 3.12, respectively. The spectral flux for kinetic energy is not significantly affected by varying Pr, especially for the vertical wavenumber spectra (Fig. 3.11, right column). For the intermediate stratifications $N = 0.15$ and 0.3, while there is a slight increase in flux with increasing Pr, the fluxes at each Pr are scarcely distinguishable between the forcing interval and dissipation range in both horizontal and vertical spectra.

The $N = 0.6$ case is different, and shows a greater dependence of $\Pi_K(k_h)$ and $\Pi_K(k_v)$

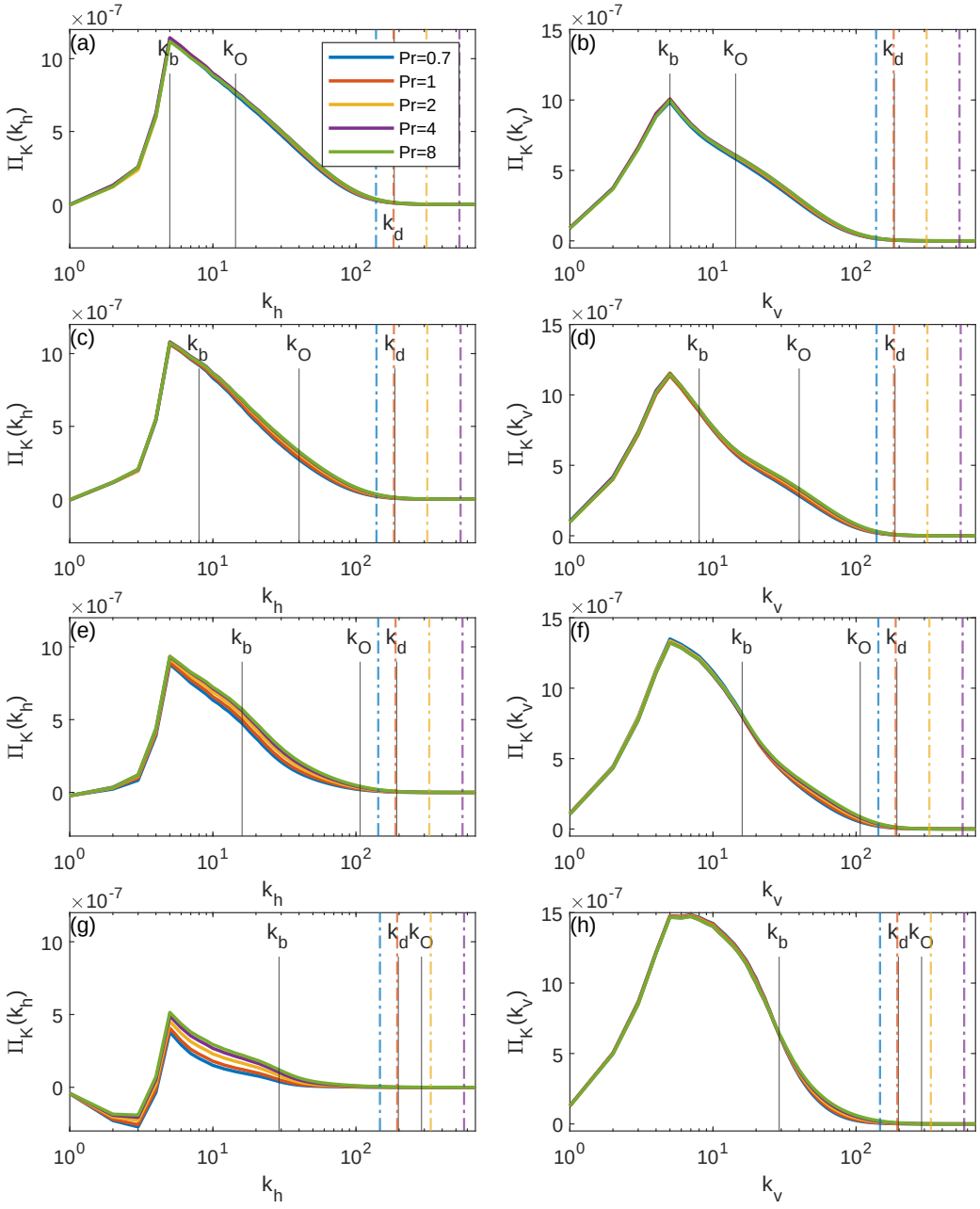

Figure 3.11: Spectral kinetic energy flux, as in equation (2.12). From top to bottom the rows are $N = 0.075$, 0.15, 0.3, and 0.6. Horizontal (left) and vertical (right) wavenumber spectra are shown. Vertical dash-dotted lines are k_θ corresponding to Pr colours.

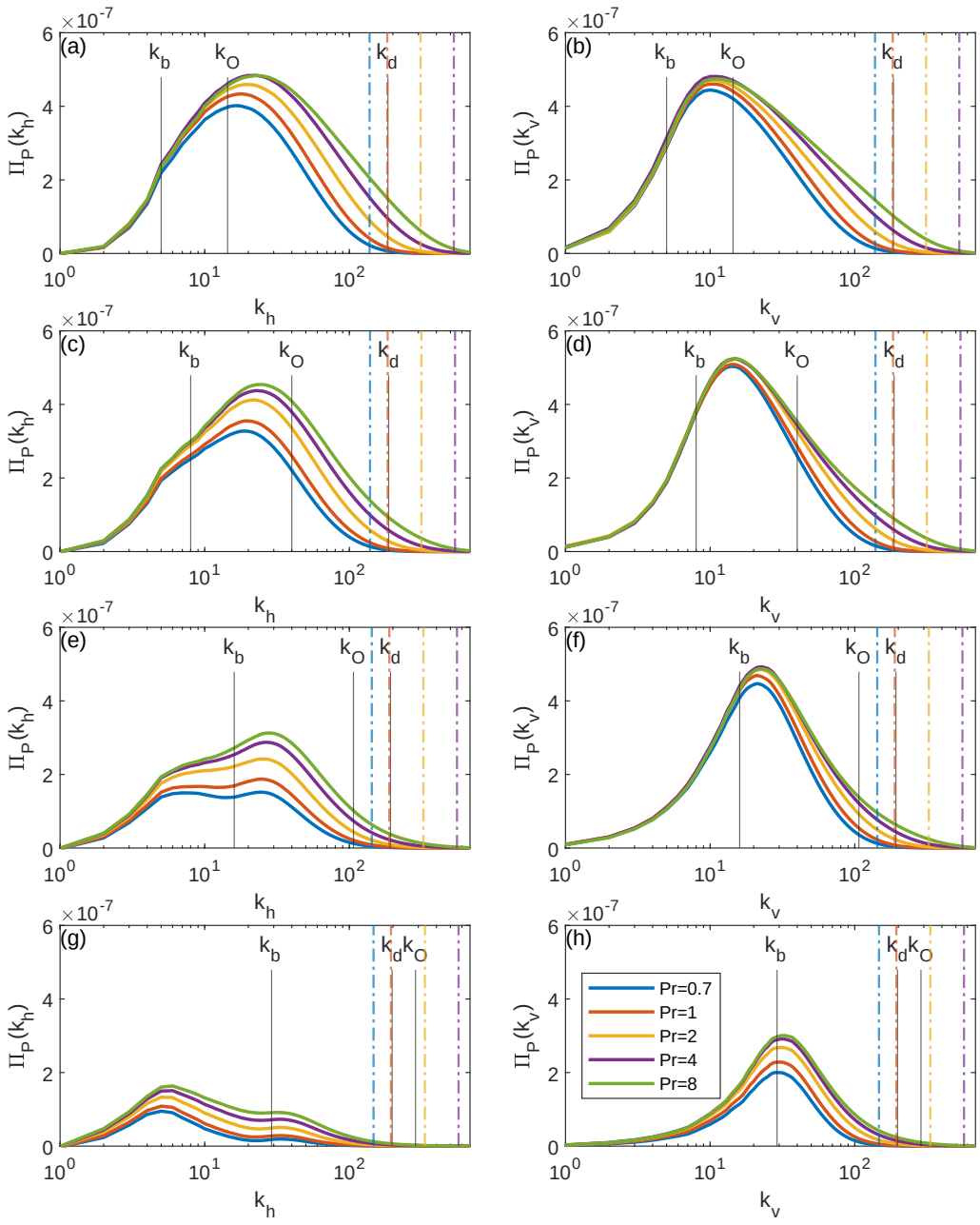

Figure 3.12: Spectral potential energy flux, as in equation (2.13). From top to bottom the rows are $N = 0.075$, 0.15, 0.3, and 0.6. Horizontal (left) and vertical (right) wavenumber spectra are shown. Vertical dash-dotted lines are k_θ corresponding to Pr colours.

on Pr. The horizontal flux $\Pi_K(k_h)$ changes with Pr at large horizontal scales (Fig. 3.11), and is the only case where the fluxes are negative for a short wavenumber range. At very small horizontal wavenumbers, upscale transfer and accumulation of energy at large scales would appear as positive $T_K(k_h)$ at small k_h, corresponding to the energy contained in vertically sheared horizontal layers when $Re_b < 1$. Downscale of the forcing interval, the Pr-dependence of $\Pi_K(k_h)$, while more apparent than at lower stratifications, is still minor. From the buoyancy flux in 3.10(g), less kinetic energy is lost by conversion to potential energy at greater Pr, slightly increasing the available kinetic energy for downscale transfer. The vertical flux $\Pi_K(k_v)$ for $N = 0.6$ is the closest to displaying a (short) constant flux range. Otherwise, varying Pr has little effect on $\Pi_K(k_v)$.

The impact of Pr on the potential energy spectral flux is more pronounced than for the kinetic flux (Fig. 3.12). In all cases, increasing Pr increases the potential energy spectral flux. From Fig. 3.9, an increase in potential energy is found with larger Pr, but for a limited wavenumber range. In the horizontal flux $\Pi_P(k_h)$ for cases $N = 0.075$, 0.15, and 0.3, the most significant change is at intermediate-to-high wavenumbers, but the large horizontal scales are still minimally affected. The $N = 0.075$ case shows Pr-dependence only for $k_h > k_b$, but for more strongly stratified cases, the Pr-dependence extends up to the forcing interval. The termination of forward potential energy flux adjusts with Pr as expected, and more potential energy is made accessible for downscale transfer at large horizontal scales, since buoyancy diffusion acts on a shorter range of associated vertical scales.

The vertical spectral fluxes are almost unaffected by Pr upscale of k_b in all but the most strongly stratified case. This is to be expected of stratified turbulence, as the buoyancy scale characterizes the horizontal layer thickness and largest vertical overturning scale; the processes responsible for potential energy transfer should be limited by k_b.

Both the horizontal and vertical potential energy fluxes are far smaller for $N = 0.6$ than the three weaker stratifications. Notably, for $N = 0.6$, the influence of Pr on the horizontal and vertical spectra persist for almost the entire wavenumber range. In the vertical flux, Pr-dependence of the potential energy flux even occurs at vertical scales larger than the layer thickness as the flow becomes more anisotropic with $Re_b < 1$. A change in Π_P would be expected when buoyancy diffusivity is weakened, but the influence of Pr extends upscale past the dissipation range in Fig. 3.12. The potential energy spectral fluxes are closer to exhibiting ranges of constant flux than for kinetic energy, but Re may still be too small for a discernable inertial range.

Again, as in the buoyancy flux spectra and energy spectra, the difference in both spectral energy fluxes between $Pr = 4$ and $Pr = 8$ is noticeably smaller than the preceding

increases of Pr. As Pr increases, Π_K and Π_K may also be expected to converge to limiting curves.

3.2.4 Physical space fields

Lastly, slices of physical space fields are examined for fixed $N = 0.3$ as Pr is increased ($Pr = 0.7$ is excluded as it is similar to the $Pr = 1$ case). Since they have fixed N, these runs have a similar $Re_b \approx 2$; the only noticeable change in the velocity, vorticity, and temperature fluctuation fields is that smaller scale features emerge as Pr increases. The changes are subtle, but close inspection of the θ field slices in Fig. 3.13 reveal the finer structures that are able to persist with larger Pr. This trend is also observed in the velocity and vorticity fields, so only the temperature and its dissipation field are shown in Figs. 3.13 and 3.14.

Vertical slices of the temperature fluctuation dissipation field are plotted in Fig. 3.14 for $Pr = 1$, 2, 4, and 8. The dissipative regions follow the horizontal layers, including the small-scale overturning and instabilities. At smaller Pr, a bigger portion of the domain is θ-dissipative and with greater intensity, since a wider range of small scales is accessible to the stronger buoyancy diffusivity. Dissipation also occurs at larger scales for smaller Pr due to a slightly smaller k_d. The dissipative regions at $Pr = 8$ are limited to extremely fine scales, which is in agreement with the largest k_θ for $N = 0.3$. Although $k_{max}/k_\theta < 1$ for the $Pr = 8$ simulations, dissipation- and diffusion- scale activity is still accounted for in these physical space fields. Larger-Pr simulations are expected to exhibit even smaller scale details in their physical fields, but will require higher resolution than $n = 1536$ used here.

3.3 Statistics and isotropy

3.3.1 Resolution and Re_b

We now look at the Pr-dependence of local isotropy through p.d.f.s and statistics of the velocity component and temperature derivative fields. The results of Pr-dependence among our simulations are then compared to those in de Bruyn Kops [2015] where the simulations had much larger Re and Re_b, but used $Pr = 1$.

There is a large difference in the resolutions of our simulations to those in de Bruyn Kops [2015]. The stratified runs in de Bruyn Kops [2015] are resolved on $8192 \times 8192 \times 4096$

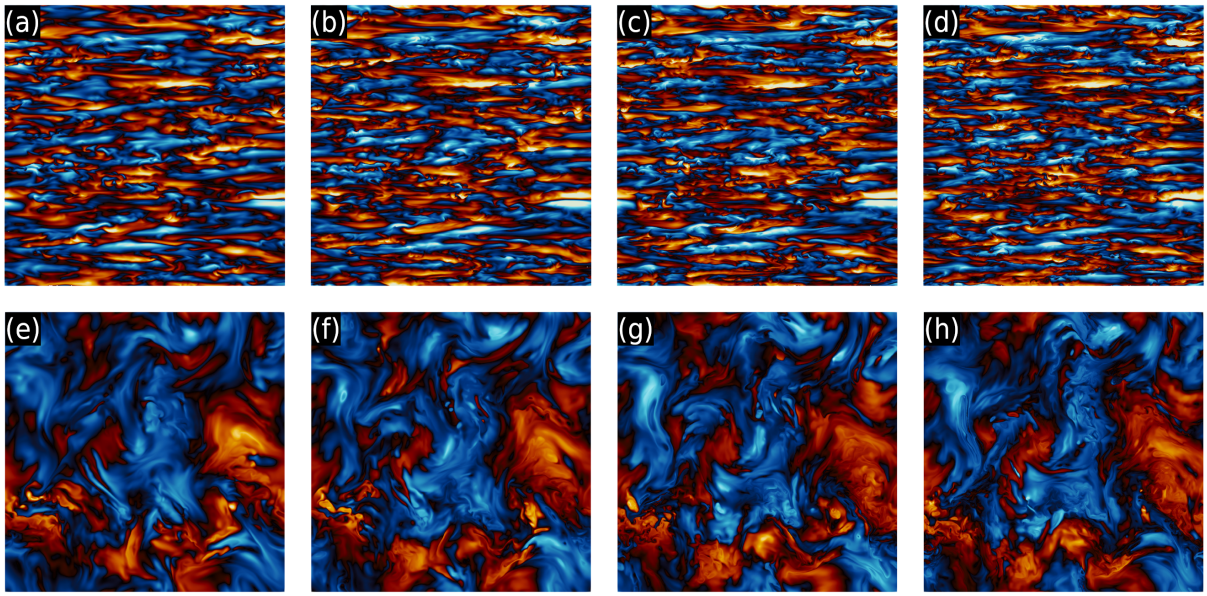

Figure 3.13: Top row: vertical slices (x, z) at $y = 0$ of θ. Bottom row: horizontal slices (x, y) at $z = 0$ of θ. Fixed $N = 0.3$ for (a,e) $Pr = 1$, (b,f) $Pr = 2$, (c,g) $Pr = 4$, and (d,h) $Pr = 8$. The same colourmap is used as in Fig. 3.2 with the range modified for visibility across Pr. The colourmap range shared by the vertical slices is different from the range shared by the horizontal slices.

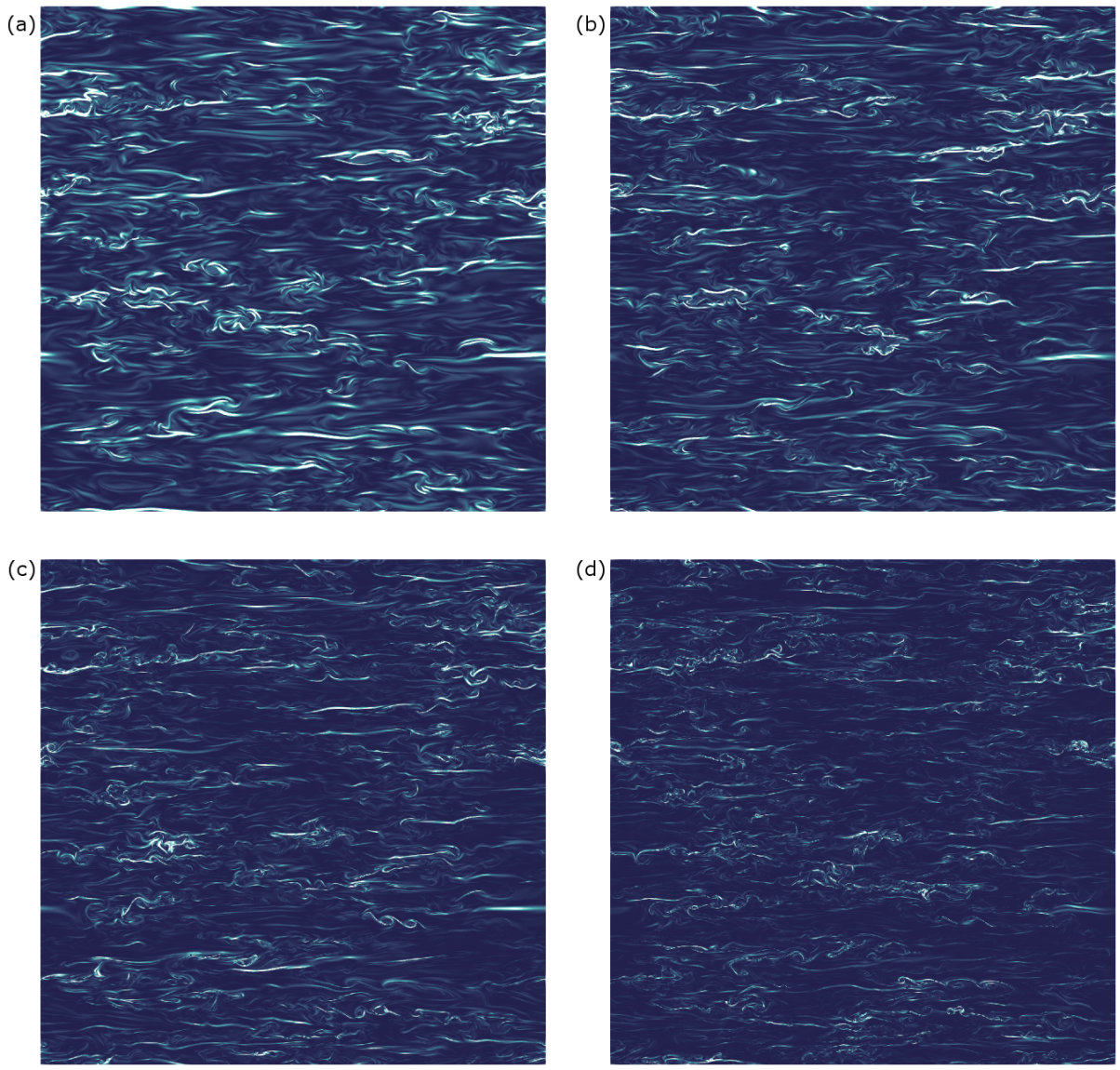

Figure 3.14: Vertical slices (x, z) at $y = 0$ of $2\kappa \frac{\partial \theta}{\partial x_j} \frac{\partial \theta}{\partial x_j}$. Fixed $N = 0.3$ for (a) $Pr = 1$, (b) $Pr = 2$, (c) $Pr = 4$, (d) $Pr = 8$. The same colourmap is used for all panels as in Fig. 3.3(b), with the range modified for visibility across Pr.

grid points while the resolution here is $1536 \times 1536 \times 1536$, which is around 80 times smaller. Dissipative scales are well resolved in each of de Bruyn Kops [2015]'s stratified runs, where $k_{max}/k_d \approx 3$; while our k_{max}/k_d is also around 3, due to various Pr in our simulations, k_{max}/k_θ ranges from about 1.2 to 5 (Table 2.1), which are still adequately resolved. Cubic domains are used here while the vertical outer direction (where 4096 points are used) in de Bruyn Kops [2015] varies with Froude number.

The resolution difference might have important consequences. In de Bruyn Kops [2015] it is stated that adequate scale separation is required for simulation results comparable to theory. The relevant scale separation in stratified turbulence simulations is related to the buoyancy Reynolds number, apparent in the form $Re_b = (k_d/k_O)^{4/3}$. The simulations presented here manage to achieve Re_b from 0.7 to 31.2, but the range is much smaller compared to $Re_b = 13$ to 220 in de Bruyn Kops [2015]. As such, our simulations may suffer from the same difficulties of the $Re_b = 13$ and 48 runs in de Bruyn Kops [2015] (e.g. poorer agreement with KOC scaling, local isotropy, local intermittency theory, etc. compared to $Re_b = 220$). Since we only examine p.d.f.s and statistics of the derivative fields, the comparatively small resolution might produce inaccurate results because of the smaller sample size in every case.

All velocity and temperature field p.d.f.s are shown in Figs. 3.15-3.28. Tables 3.2, 3.4, 3.6, and 3.8 contain all moment data on velocity derivatives while Tables 3.3, 3.5, 3.7, and 3.9 contain all moment data on temperature derivatives. To review, the observations of the moments and p.d.f.s in de Bruyn Kops [2015] for $Pr = 1$ were that (1) velocity derivatives p.d.f. shapes depart from the isotropic benchmark as stratification strength is increased: in the strongest cases, $u_{1,3}$ becomes similar to the isotropic case while $u_{3,1}$ develops a sharp peak near zero, and (2) stratification tends to increase all scalar derivative kurtoses; vertical derivatives of the scalar were larger than horizontal derivatives. Our simulations at each Pr were consistent with these stratification-dependent results in de Bruyn Kops [2015]; below, the results will focus on Pr-dependence in the p.d.f.s and statistics.

	Run	$u_{1,1}$	$u_{2,2}$	$u_{3,3}$	$u_{1,2}$	$u_{1,3}$	$u_{2,1}$	$u_{2,3}$	$u_{3,1}$	$u_{3,2}$
	A0	0.0091	0.0092	0.0110	0.0168	0.0260	0.0162	0.0257	0.0173	0.0176
	A1	0.0096	0.0096	0.0116	0.0173	0.0267	0.0171	0.0267	0.0187	0.0190
σ^2	A2	0.0100	0.0100	0.0123	0.0179	0.0275	0.0178	0.0275	0.0204	0.0206
	A3	0.0103	0.0103	0.0129	0.0183	0.0281	0.0181	0.0279	0.0219	0.0219
	A0	-0.5583	-0.5649	-0.4599	0.0191	-0.0082	0.0131	-0.0277	-0.0230	0.0113
	A1	-0.5560	-0.5480	-0.4576	0.0052	0.0015	0.0277	-0.0747	-0.0012	0.0375
S	A2	-0.5513	-0.5410	-0.4508	0.0149	0.0097	0.0441	-0.0302	0.0048	0.0127
	A3	-0.5333	-0.5304	-0.4504	-0.0236	-0.0226	0.0106	-0.0299	-0.0027	0.0121
	A0	6.7318	6.7496	5.9988	9.8065	8.0542	9.7921	8.2244	9.9002	9.8656
	A1	6.5532	6.5648	5.8310	9.4334	7.9550	9.6222	8.0920	9.3985	9.6277
K	A2	6.4161	6.3711	5.7009	9.3721	7.8746	9.4072	7.9517	8.9769	8.9766
	A3	6.1834	6.1710	5.5809	8.8887	7.8276	8.9057	7.8783	8.4862	8.4153

Table 3.2: Variance σ^2, skewness S, and kurtosis K of velocity derivatives for $N = 0.075$.

	Run	$\theta_{,1}$	$\theta_{,2}$	$\theta_{,3}$
	A0	0.0159	0.0163	0.0256
	A1	0.0223	0.0227	0.0346
σ^2	A2	0.0411	0.0415	0.0609
	A3	0.0759	0.0763	0.1081
	A0	0.0634	-0.0042	1.4835
	A1	0.0328	-0.1063	1.3712
S	A2	-0.0032	-0.0208	1.1609
	A3	0.0005	-0.0172	0.8699
	A0	15.1719	15.1223	13.0020
	A1	16.3245	16.4094	13.8050
K	A2	19.7576	19.4123	16.4443
	A3	20.9514	20.7440	18.0925

Table 3.3: Variance σ^2, skewness S, and kurtosis K of $\theta_{,j}$ for $N = 0.075$.

	Run	$u_{1,1}$	$u_{2,2}$	$u_{3,3}$	$u_{1,2}$	$u_{1,3}$	$u_{2,1}$	$u_{2,3}$	$u_{3,1}$	$u_{3,2}$
	B0	0.0083	0.0083	0.0117	0.0133	0.0376	0.0133	0.0377	0.0146	0.0145
	B1	0.0088	0.0088	0.0125	0.0140	0.0385	0.0138	0.0384	0.0159	0.0159
σ^2	B2	0.0096	0.0096	0.0139	0.0152	0.0403	0.0150	0.0402	0.0184	0.0185
	B3	0.0102	0.0103	0.0150	0.0160	0.0414	0.0158	0.0416	0.0206	0.0207
	B0	-0.6256	-0.6242	-0.3379	0.0119	0.0085	0.0566	0.0068	-0.0007	0.0115
	B1	-0.6207	-0.6133	-0.3297	0.0040	0.0140	0.0519	-0.0102	-0.0039	0.0035
S	B2	-0.6259	-0.5979	-0.3156	0.0364	0.0083	0.0381	-0.0258	0.0041	0.0040
	B3	-0.6068	-0.6036	-0.3000	0.0260	0.0049	0.0224	-0.0064	-0.0052	-0.0019
	B0	8.7727	8.6898	6.9122	13.1036	7.0222	13.2204	6.9558	14.2824	13.9475
	B1	8.4003	8.3641	6.6841	12.6449	6.9901	12.3717	6.9460	12.9558	13.0473
K	B2	8.1846	8.0502	6.5058	12.1622	6.9818	12.0207	6.9560	12.5014	12.3554
	B3	7.8498	7.8734	6.3768	11.5775	7.0059	11.2681	6.9277	11.4995	11.5417

Table 3.4: Variance σ^2, skewness S, and kurtosis K of velocity derivatives for $N = 0.15$.

	Run	$\theta_{,1}$	$\theta_{,2}$	$\theta_{,3}$
	B0	0.0128	0.0128	0.0360
	B1	0.0166	0.0169	0.0456
σ^2	B2	0.0285	0.0289	0.0723
	B3	0.0497	0.0501	0.1175
	B0	-0.0145	-0.0129	1.4260
	B1	-0.0158	0.0178	1.4985
S	B2	0.0449	-0.0442	1.5334
	B3	0.0107	-0.0736	1.4020
	B0	18.0630	17.6504	10.0816
	B1	18.8581	19.3523	11.3806
K	B2	26.3386	25.1690	14.7348
	B3	29.1204	28.9173	18.1033

Table 3.5: Variance σ^2, skewness S, and kurtosis K of $\theta_{,j}$ for $N = 0.15$.

	Run	$u_{1,1}$	$u_{2,2}$	$u_{3,3}$	$u_{1,2}$	$u_{1,3}$	$u_{2,1}$	$u_{2,3}$	$u_{3,1}$	$u_{3,2}$
	C0	0.0054	0.0054	0.0086	0.0079	0.0649	0.0073	0.0629	0.0072	0.0075
	C1	0.0060	0.0060	0.0097	0.0086	0.0664	0.0081	0.0646	0.0086	0.0087
σ^2	C2	0.0071	0.0071	0.0117	0.0099	0.0698	0.0093	0.0686	0.0109	0.0110
	C3	0.0079	0.0080	0.0133	0.0110	0.0719	0.0104	0.0708	0.0129	0.0132
	C0	-0.8537	-0.8373	-0.1394	-0.1876	0.0068	0.0873	-0.0232	-0.0522	0.0185
	C1	-0.8402	-0.8125	-0.1259	-0.1278	0.0046	0.0498	-0.0252	0.0044	-0.0211
S	C2	-0.8161	-0.7872	-0.1184	-0.1028	0.0031	0.0543	-0.0199	-0.0087	0.0006
	C3	-0.7711	-0.7797	-0.1188	-0.1234	0.0030	0.0224	-0.0137	0.0076	-0.0133
	C0	16.3664	16.3058	11.6563	25.7567	6.0566	24.0127	5.8659	34.7644	36.8724
	C1	15.3797	15.0442	10.7445	24.7708	6.1397	23.1483	5.9223	30.6398	29.8842
K	C2	14.4911	14.1859	10.1062	24.2949	6.2722	21.3554	6.0131	27.2880	28.7539
	C3	13.2774	13.6789	9.6516	21.5470	6.3150	20.1179	6.1853	24.7725	25.9838

Table 3.6: Variance σ^2, skewness S, and kurtosis K of velocity derivatives for $N = 0.3$.

	Run	$\theta_{,1}$	$\theta_{,2}$	$\theta_{,3}$
	C0	0.0070	0.0073	0.0475
	C1	0.0092	0.0094	0.0591
σ^2	C2	0.0146	0.0150	0.0886
	C3	0.0233	0.0240	0.1298
	C0	-0.0281	-0.0209	1.0286
	C1	0.0198	0.0087	1.1558
S	C2	0.0140	-0.0379	1.4221
	C3	0.0661	0.0028	1.6062
	C0	25.6128	28.0372	6.9086
	C1	29.8049	31.6684	7.8276
K	C2	42.6660	47.1741	11.0269
	C3	55.7695	59.2872	14.6095

Table 3.7: Variance σ^2, skewness S, and kurtosis K of $\theta_{,j}$ for $N = 0.3$.

	Run	$u_{1,1}$	$u_{2,2}$	$u_{3,3}$	$u_{1,2}$	$u_{1,3}$	$u_{2,1}$	$u_{2,3}$	$u_{3,1}$	$u_{3,2}$
	D0	0.0015	0.0015	0.0019	0.0028	0.0878	0.0027	0.0846	0.0009	0.0008
	D1	0.0018	0.0017	0.0024	0.0030	0.0908	0.0029	0.0876	0.0013	0.0012
σ^2	D2	0.0023	0.0023	0.0035	0.0035	0.0957	0.0034	0.0931	0.0021	0.0021
	D3	0.0027	0.0028	0.0044	0.0040	0.0998	0.0038	0.0972	0.0028	0.0028
	D0	-0.9951	-0.9288	0.2655	0.1545	-0.0044	-0.1538	-0.0581	-0.0884	0.5370
	D1	-1.0296	-0.9968	0.2346	0.1773	-0.0015	-0.1104	-0.0502	-0.1411	0.1857
S	D2	-1.0175	-0.9864	0.1416	0.0786	-0.0046	-0.1570	-0.0503	-0.0782	0.0655
	D3	-1.0175	-0.9455	0.0945	0.0270	-0.0024	-0.0722	-0.0483	0.0645	-0.0227
	D0	26.2281	23.2829	33.6454	17.3488	5.0816	23.6842	4.9327	267.5192	172.5735
	D1	28.6352	25.2961	32.1450	20.7005	5.0999	26.7093	4.9516	215.0309	148.3986
K	D2	28.4126	26.3294	26.8929	25.0506	5.1940	31.2766	5.0771	156.5756	117.8833
	D3	27.2736	26.2379	23.7782	26.8933	5.2434	31.8050	5.1662	119.0278	99.8968

Table 3.8: Variance σ^2, skewness S, and kurtosis K of velocity derivatives for $N = 0.6$.

	Run	$\theta_{,1}$	$\theta_{,2}$	$\theta_{,3}$
	D0	0.0015	0.0015	0.0442
	D1	0.0021	0.0020	0.0551
σ^2	D2	0.0034	0.0034	0.0796
	D3	0.0050	0.0051	0.1078
	D0	-0.2581	0.0634	0.4533
	D1	-0.3896	0.0316	0.5314
S	D2	-0.2954	-0.1107	0.7052
	D3	-0.3500	-0.1141	0.8934
	D0	63.8036	44.5879	4.8271
	D1	79.3574	67.7154	5.3414
K	D2	119.7340	93.1336	6.7255
	D3	158.8522	124.7120	8.6415

Table 3.9: Variance σ^2, skewness S, and kurtosis K of $\theta_{,j}$ for $N = 0.6$.

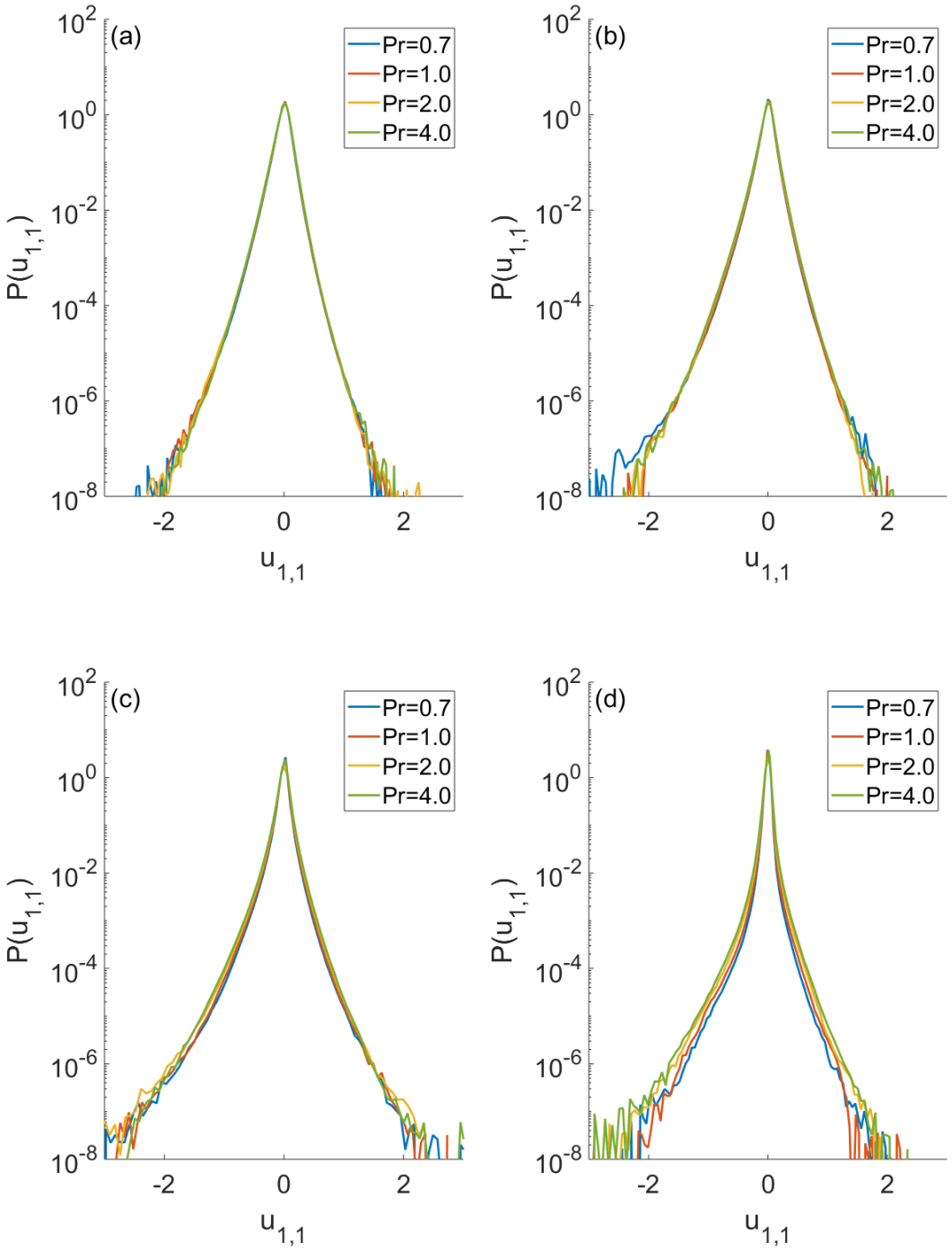

Figure 3.15: Velocity derivative p.d.f.s ($u_{1,1}$) with (a) N=0.075, (b) N=0.15, (c) N=0.3, and (d) N=0.6.

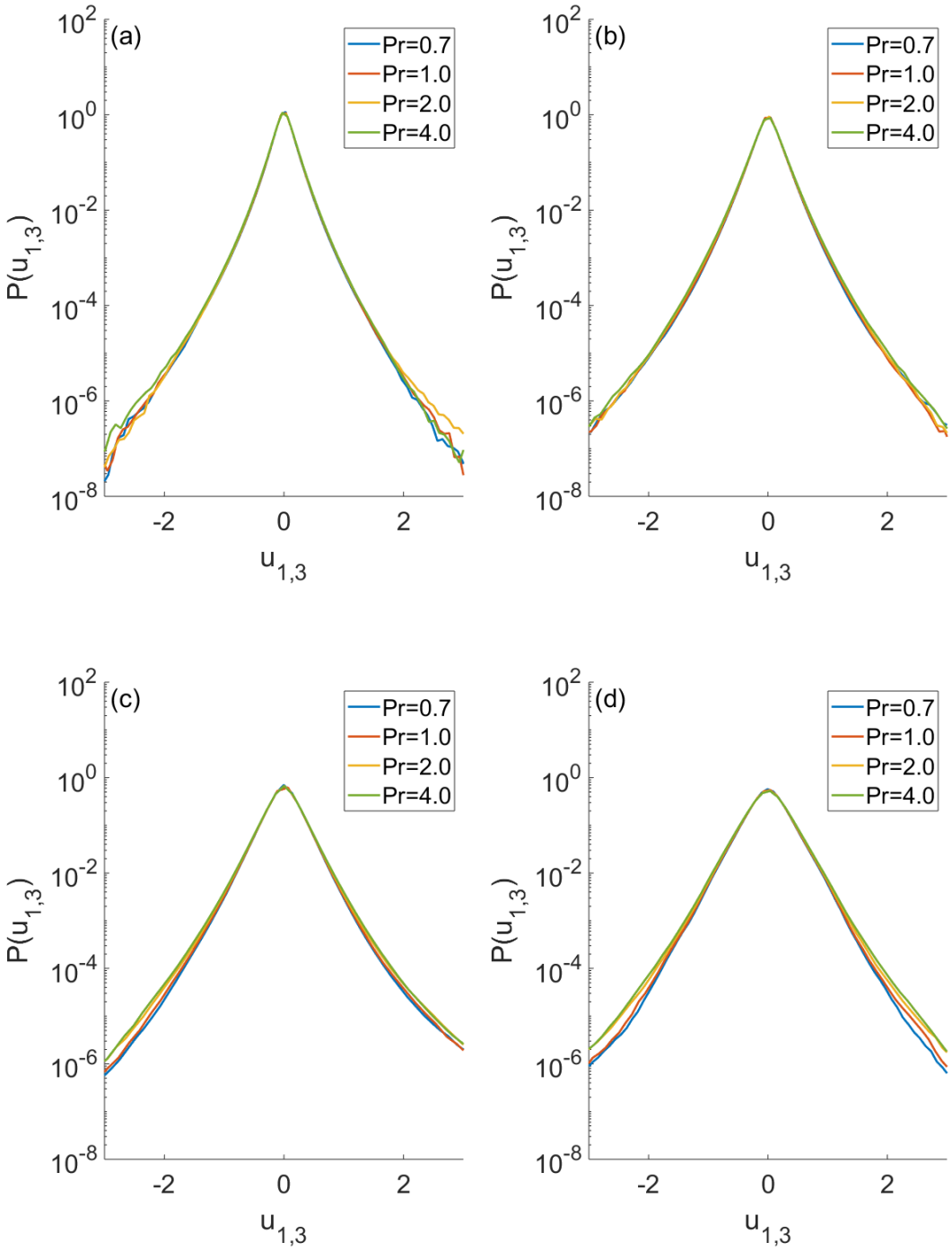

Figure 3.16: Velocity derivative p.d.f.s ($u_{1,3}$) with (a) N=0.075, (b) N=0.15, (c) N=0.3, and (d) N=0.6.

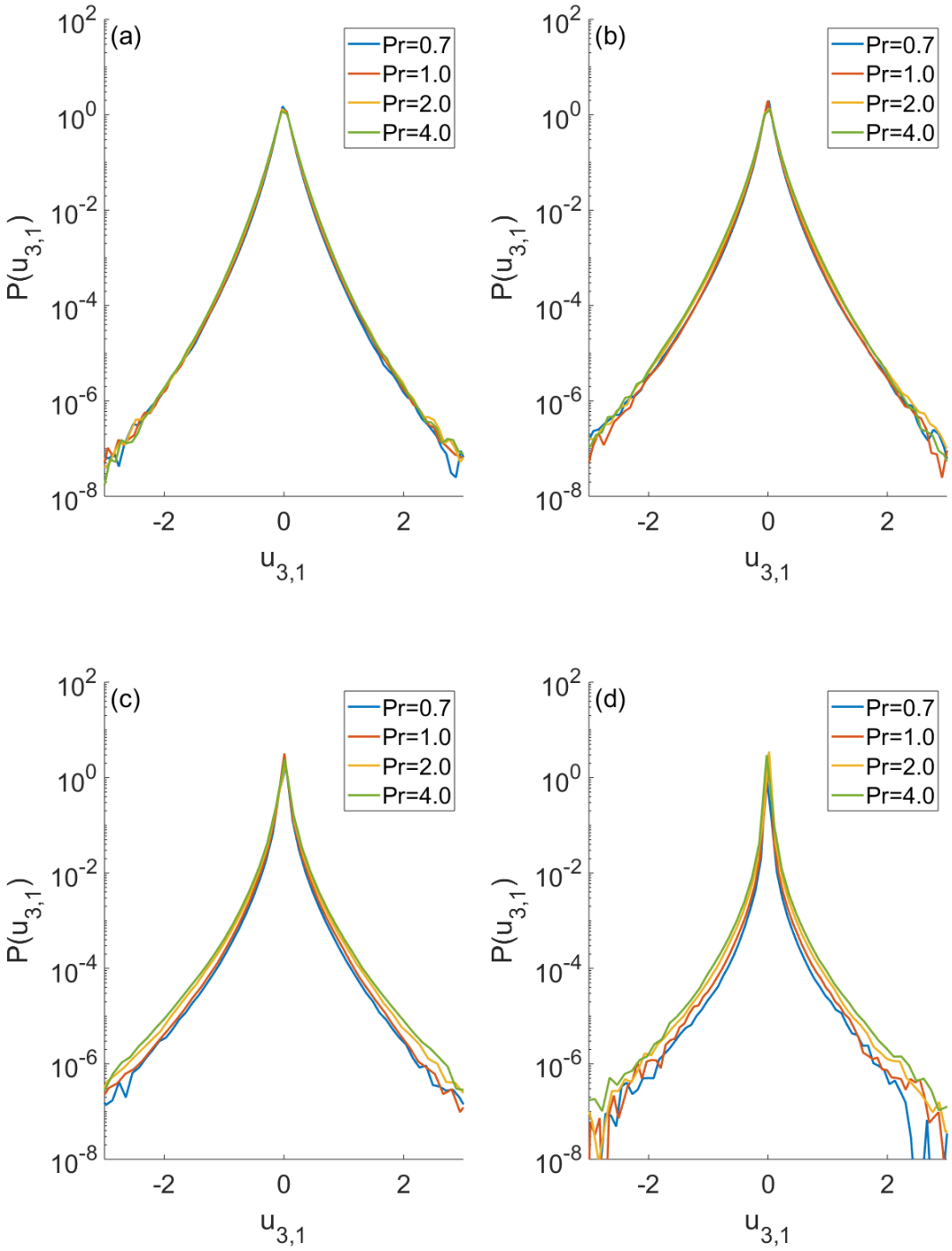

Figure 3.17: Velocity derivative p.d.f.s ($u_{3,1}$) with (a) N=0.075, (b) N=0.15, (c) N=0.3, and (d) N=0.6.

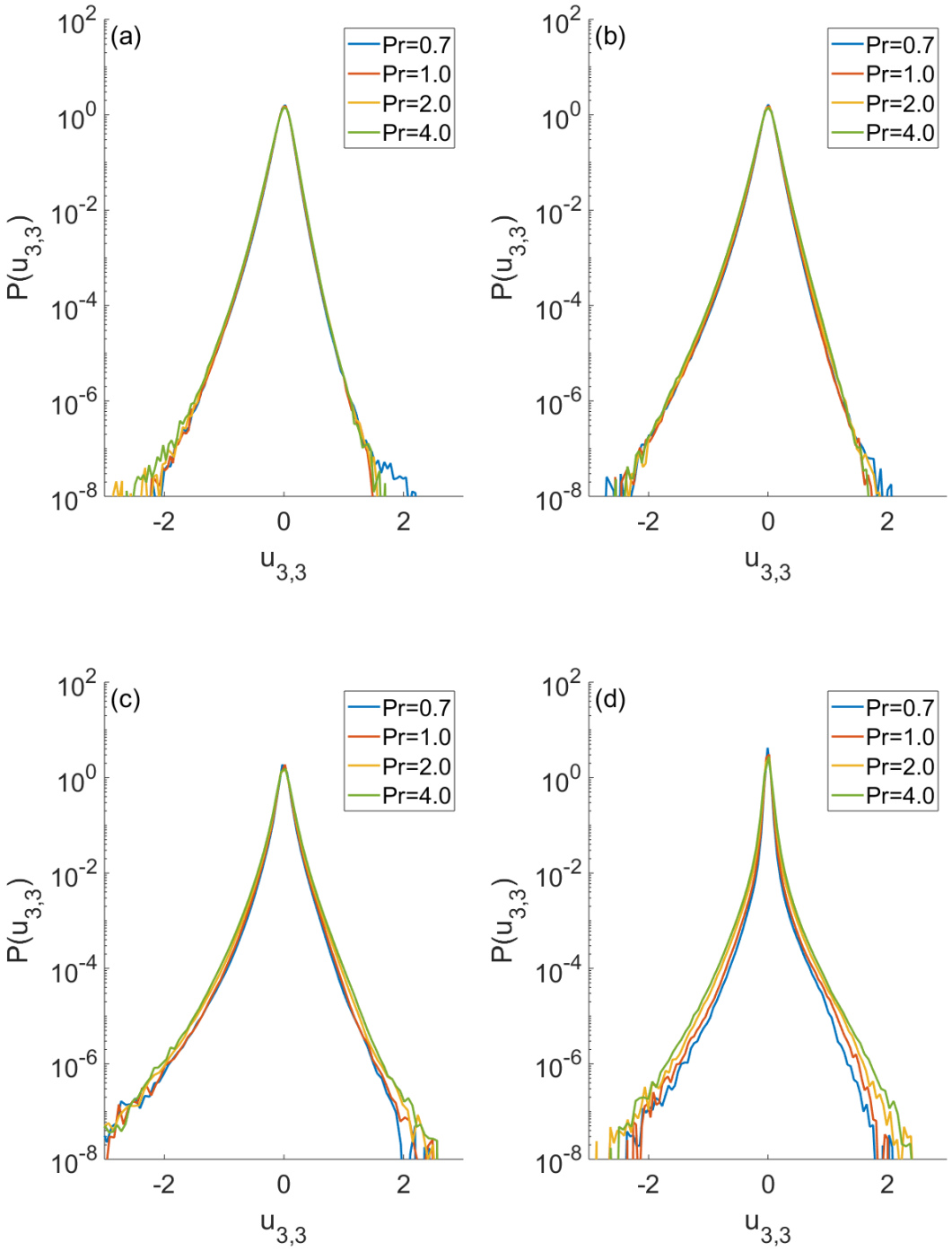

Figure 3.18: Velocity derivative p.d.f.s ($u_{3,3}$) with (a) N=0.075, (b) N=0.15, (c) N=0.3, and (d) N=0.6.

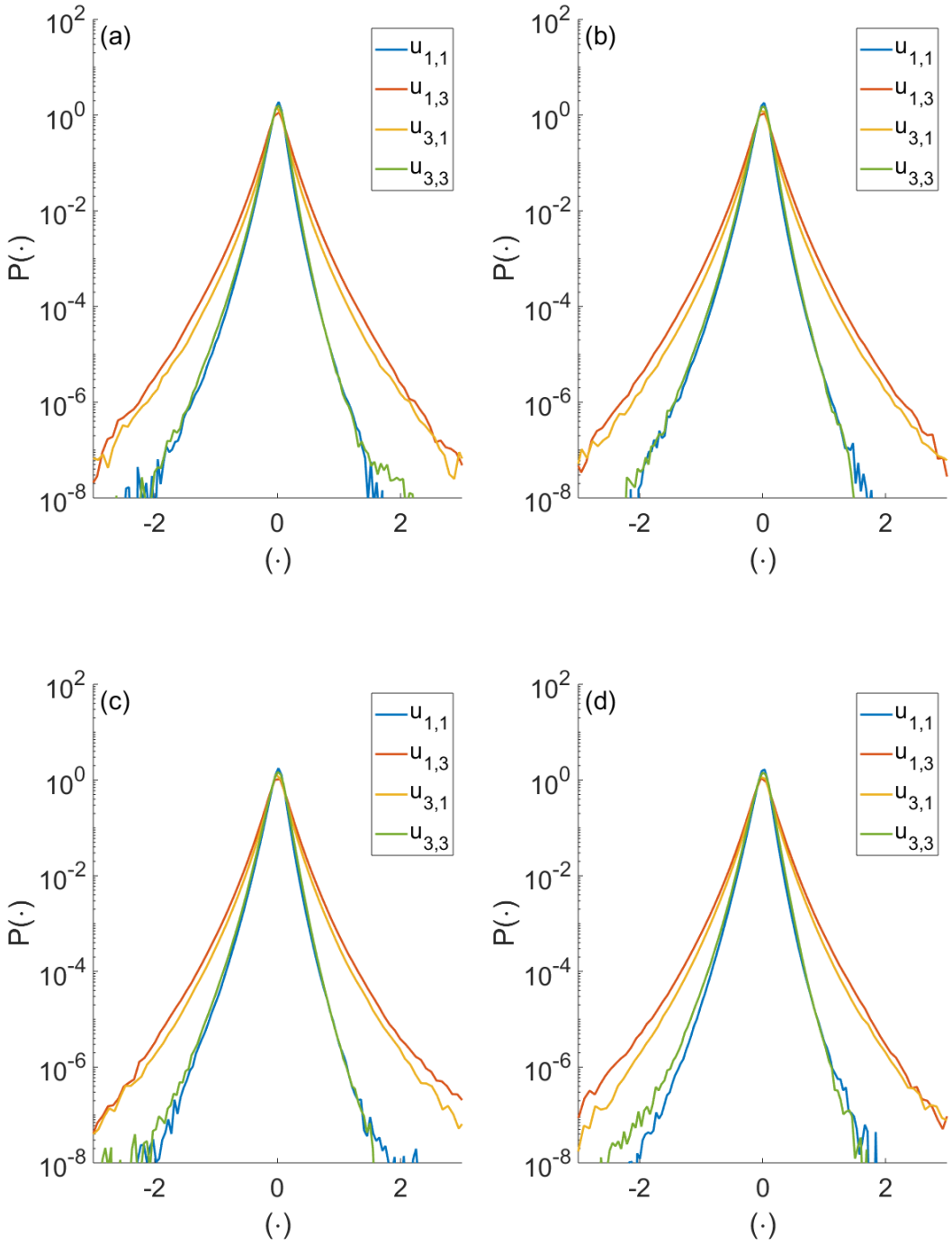

Figure 3.19: Velocity derivative p.d.f.s for N=0.075 with (a) Pr=0.7, (b) Pr=1, (c) Pr=2, and (d) Pr=4.

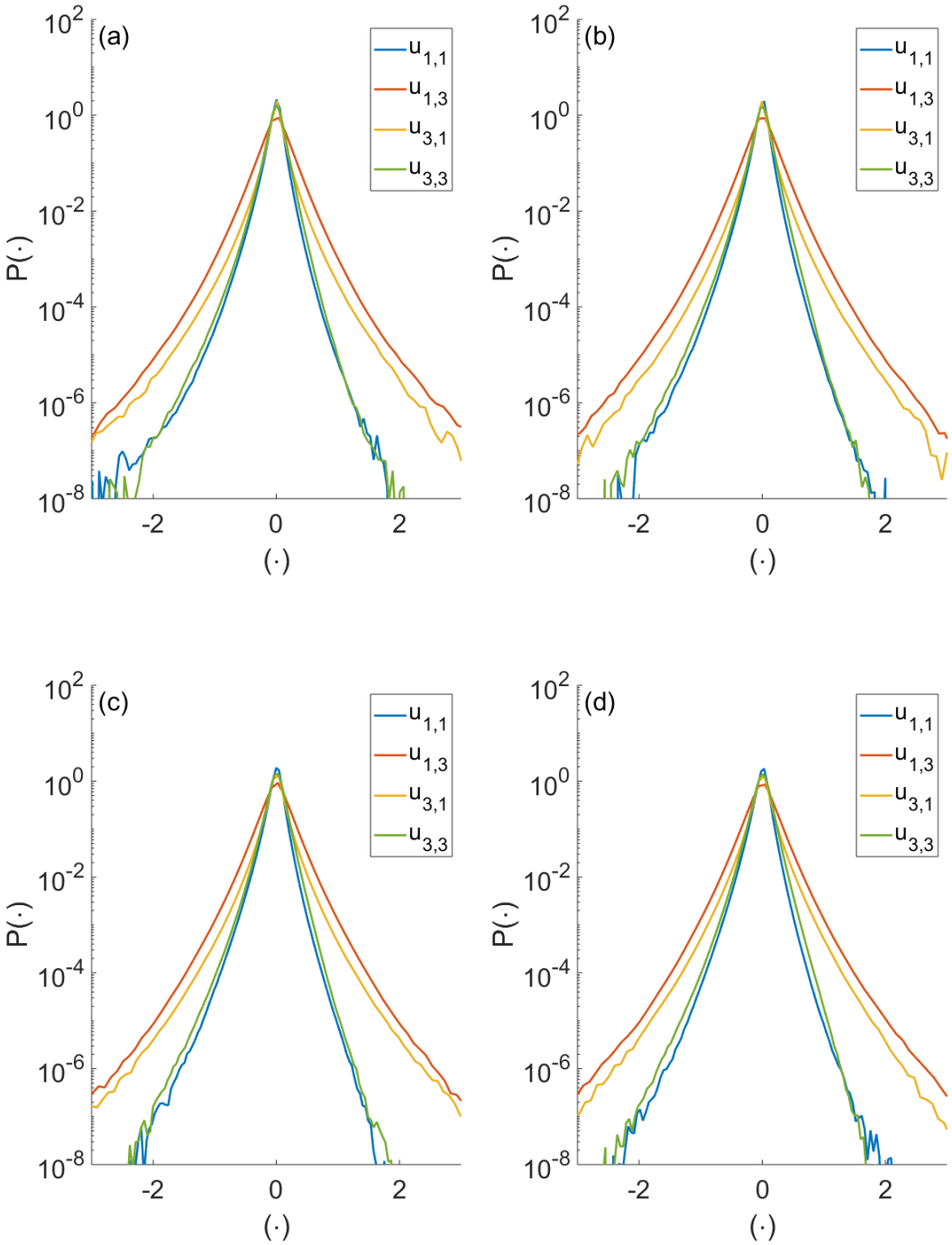

Figure 3.20: Velocity derivative p.d.f.s for N=0.15 with (a) Pr=0.7, (b) Pr=1, (c) Pr=2, and (d) Pr=4.

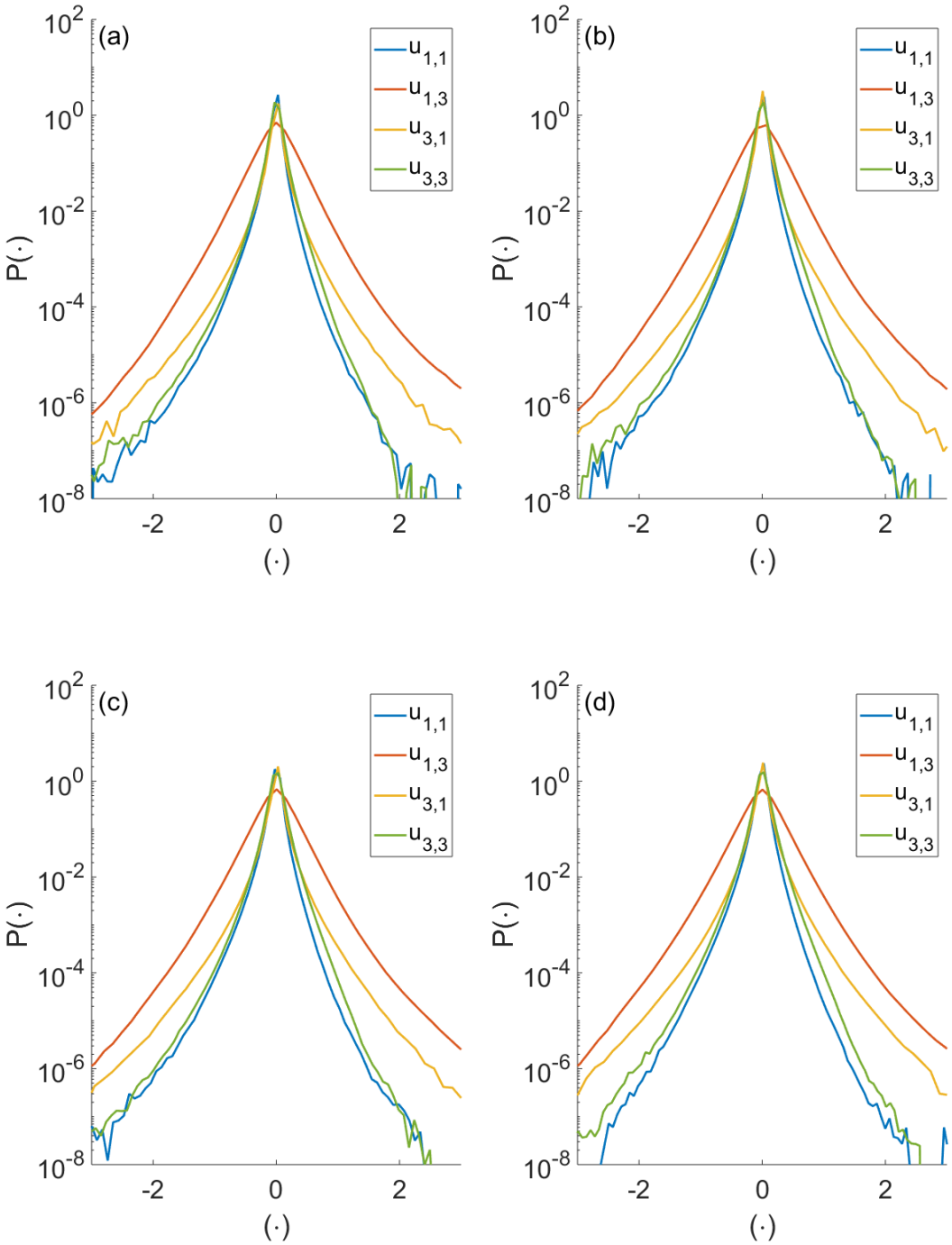

Figure 3.21: Velocity derivative p.d.f.s for N=0.3 with (a) Pr=0.7, (b) Pr=1, (c) Pr=2, and (d) Pr=4.

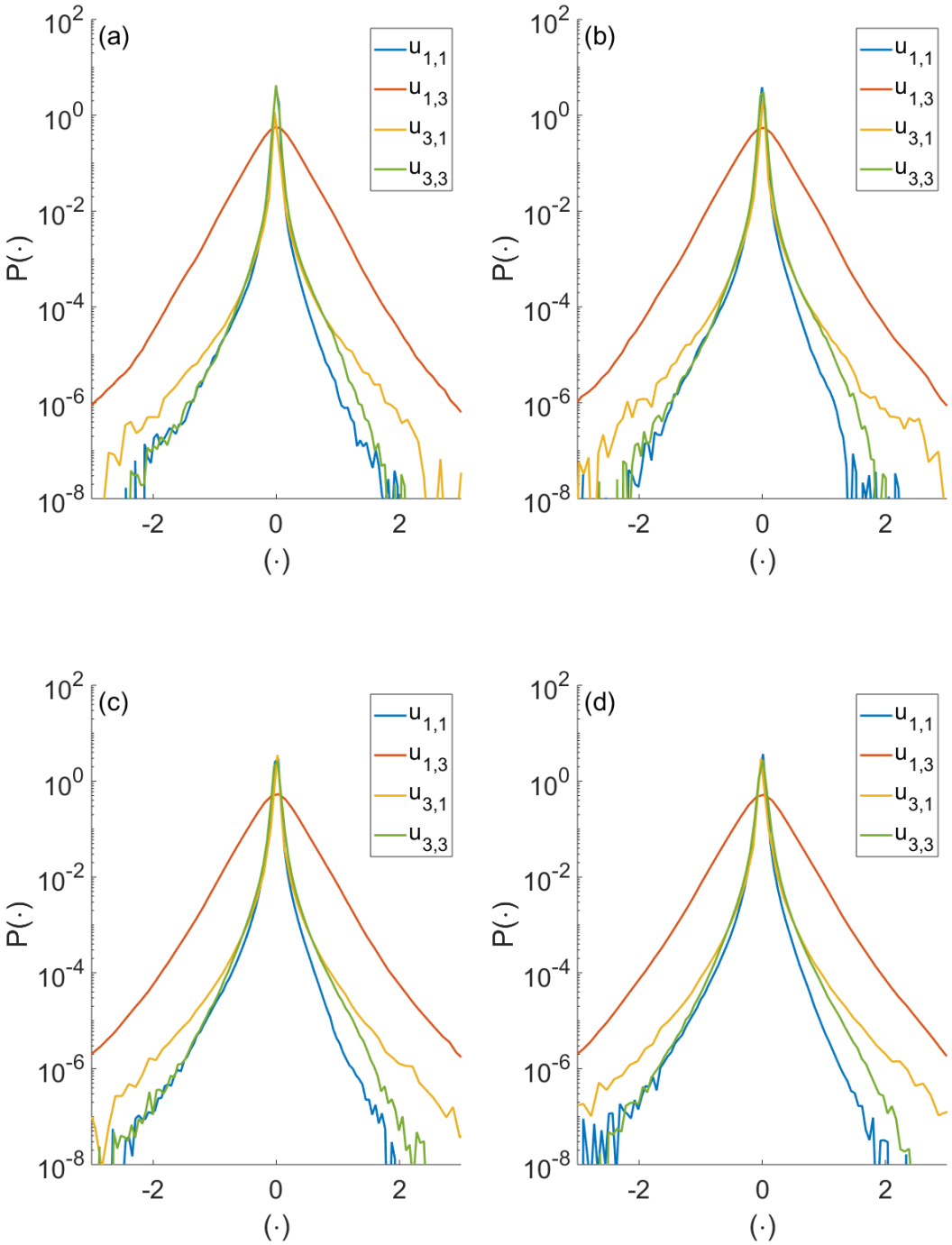

Figure 3.22: Velocity derivative p.d.f.s for N=0.6 with (a) Pr=0.7, (b) Pr=1, (c) Pr=2, and (d) Pr=4.

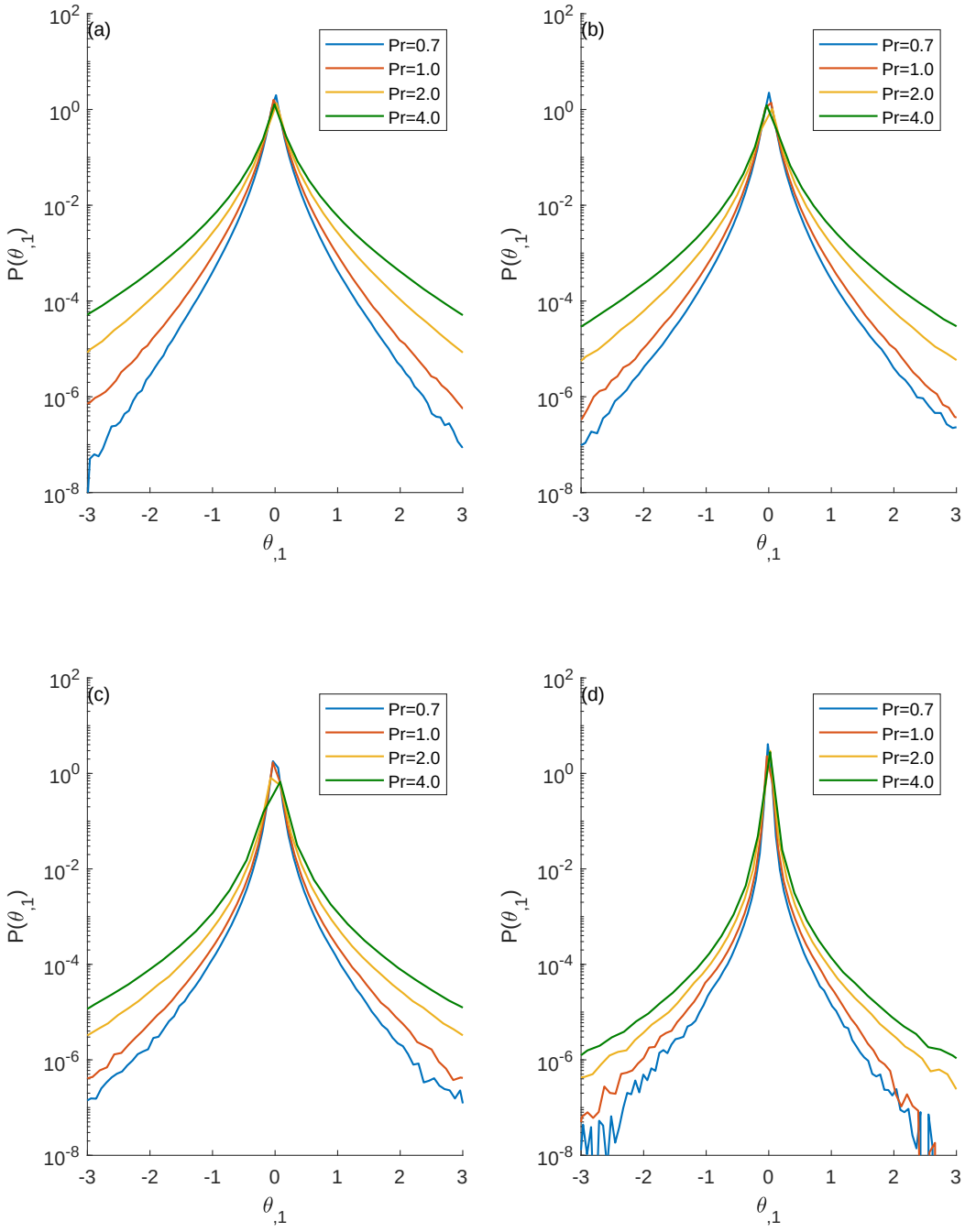

Figure 3.23: Temperature derivative p.d.f.s $\theta_{,1}$ with (a) N=0.075, (b) N=0.15, (c) N=0.3, and (d) N=0.6.

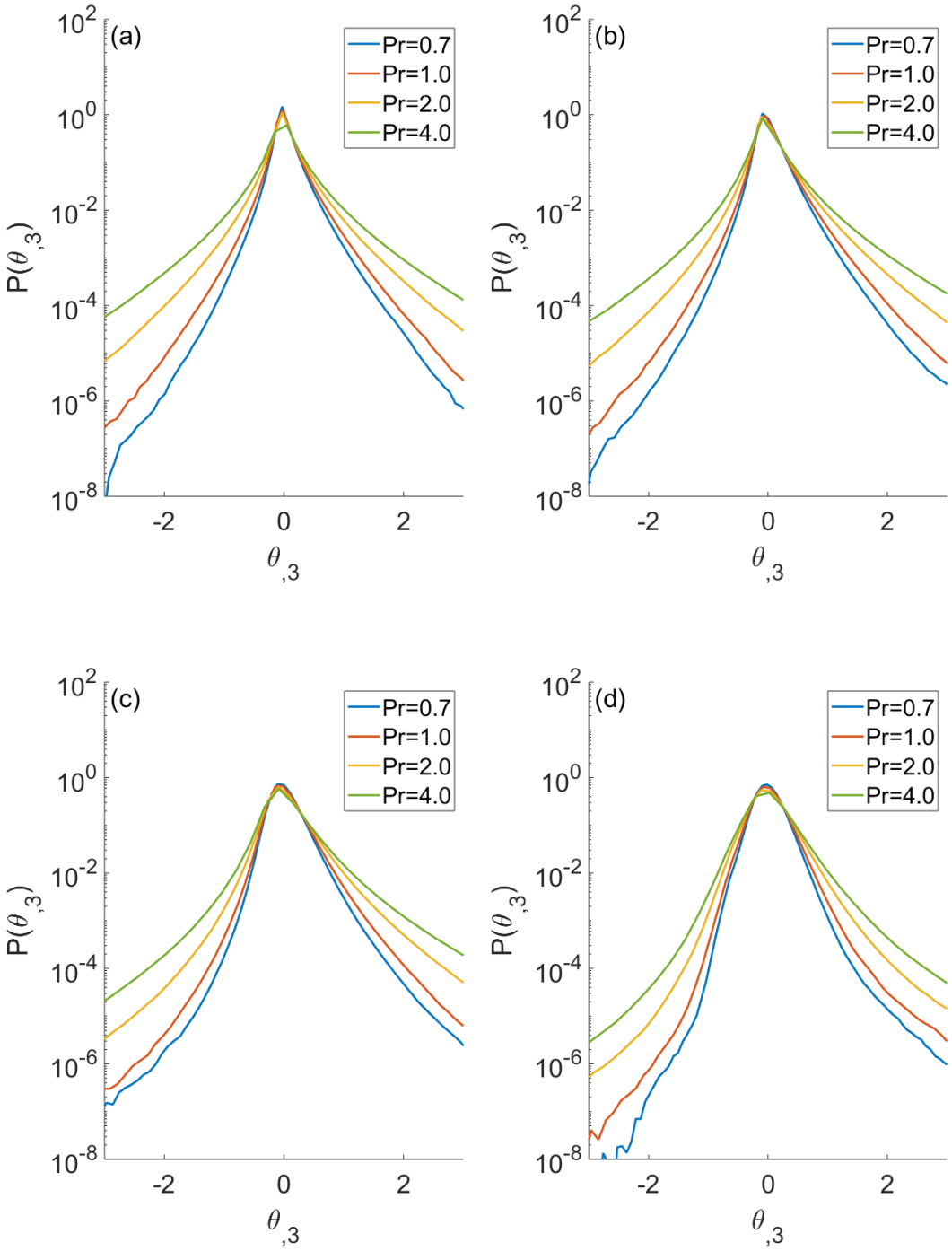

Figure 3.24: Temperature derivative p.d.f.s $\theta_{,3}$ with (a) N=0.075, (b) N=0.15, (c) N=0.3, and (d) N=0.6.

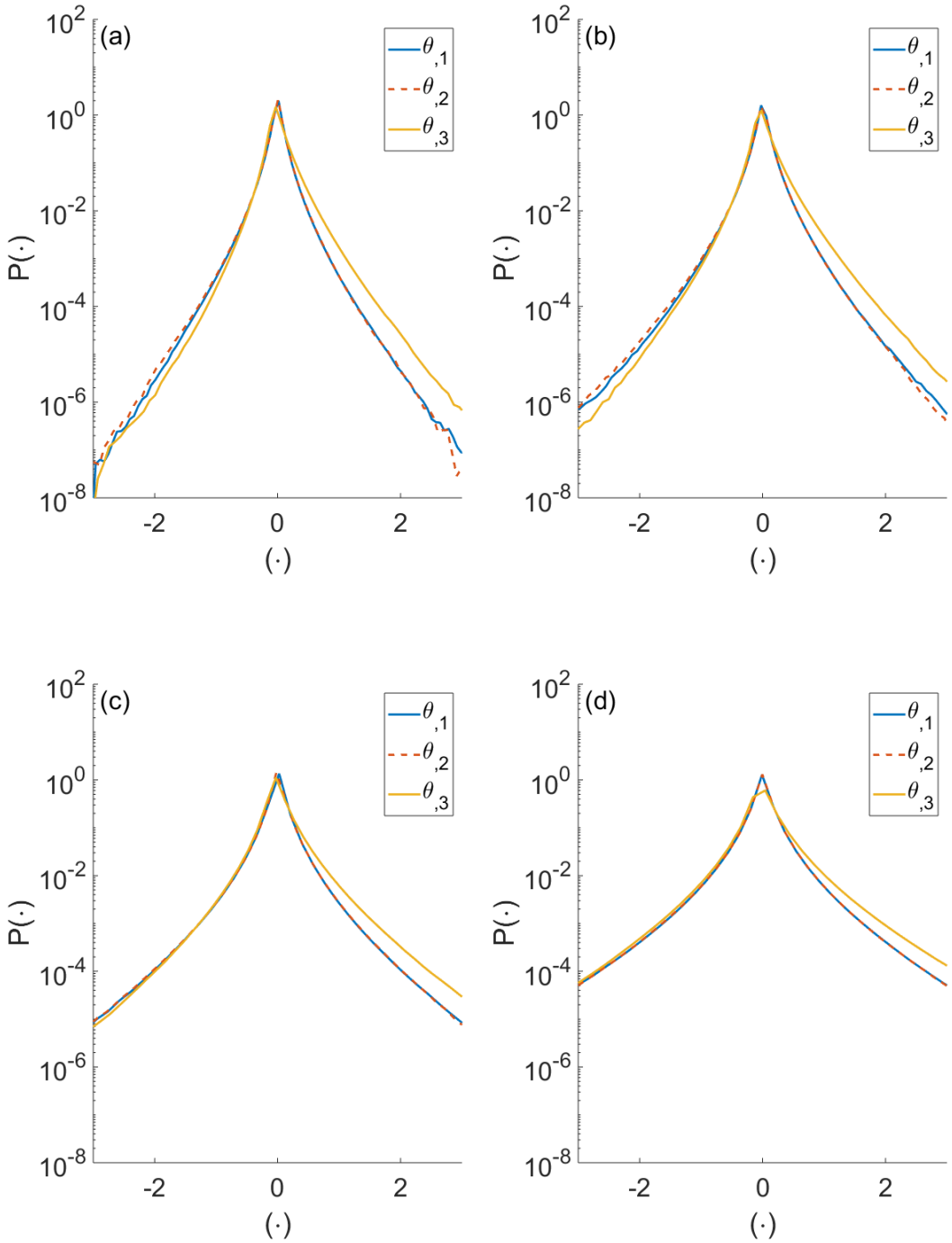

Figure 3.25: Temperature derivative p.d.f.s for N=0.075 with (a) Pr=0.7, (b) Pr=1, (c) Pr=2, and (d) Pr=4.

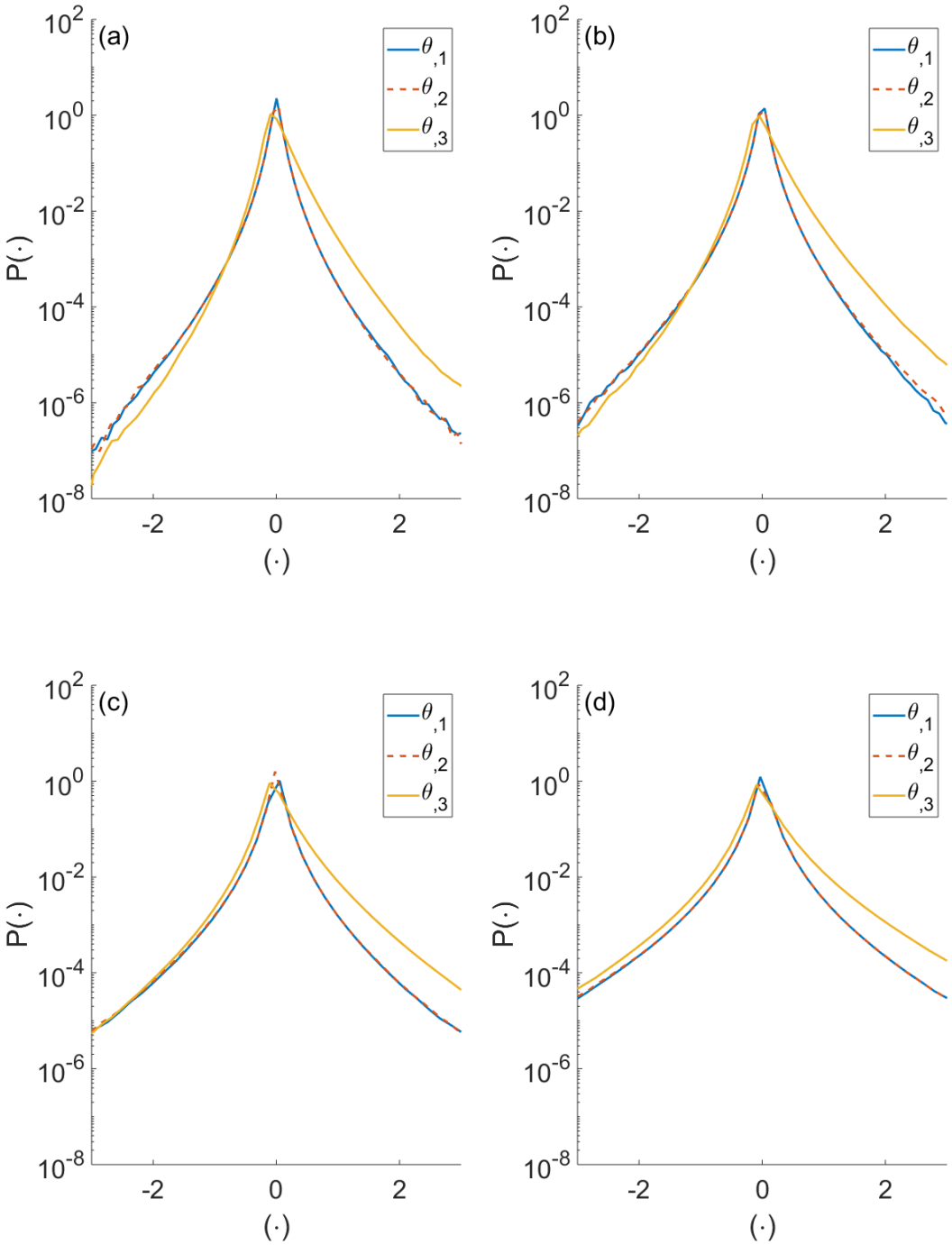

Figure 3.26: Temperature derivative p.d.f.s for N=0.15 with (a) Pr=0.7, (b) Pr=1, (c) Pr=2, and (d) Pr=4.

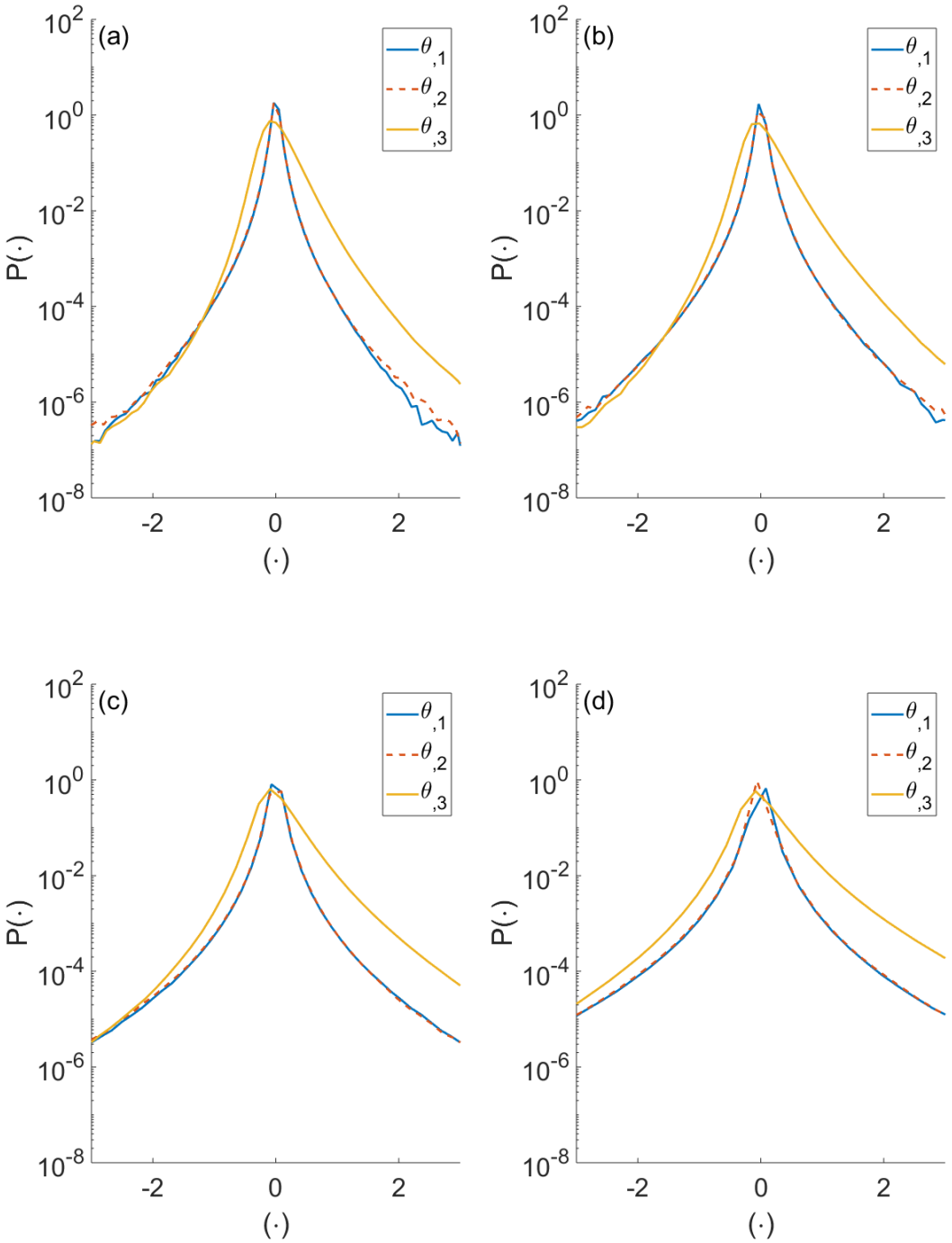

Figure 3.27: Temperature derivative p.d.f.s for N=0.3 with (a) Pr=0.7, (b) Pr=1, (c) Pr=2, and (d) Pr=4.

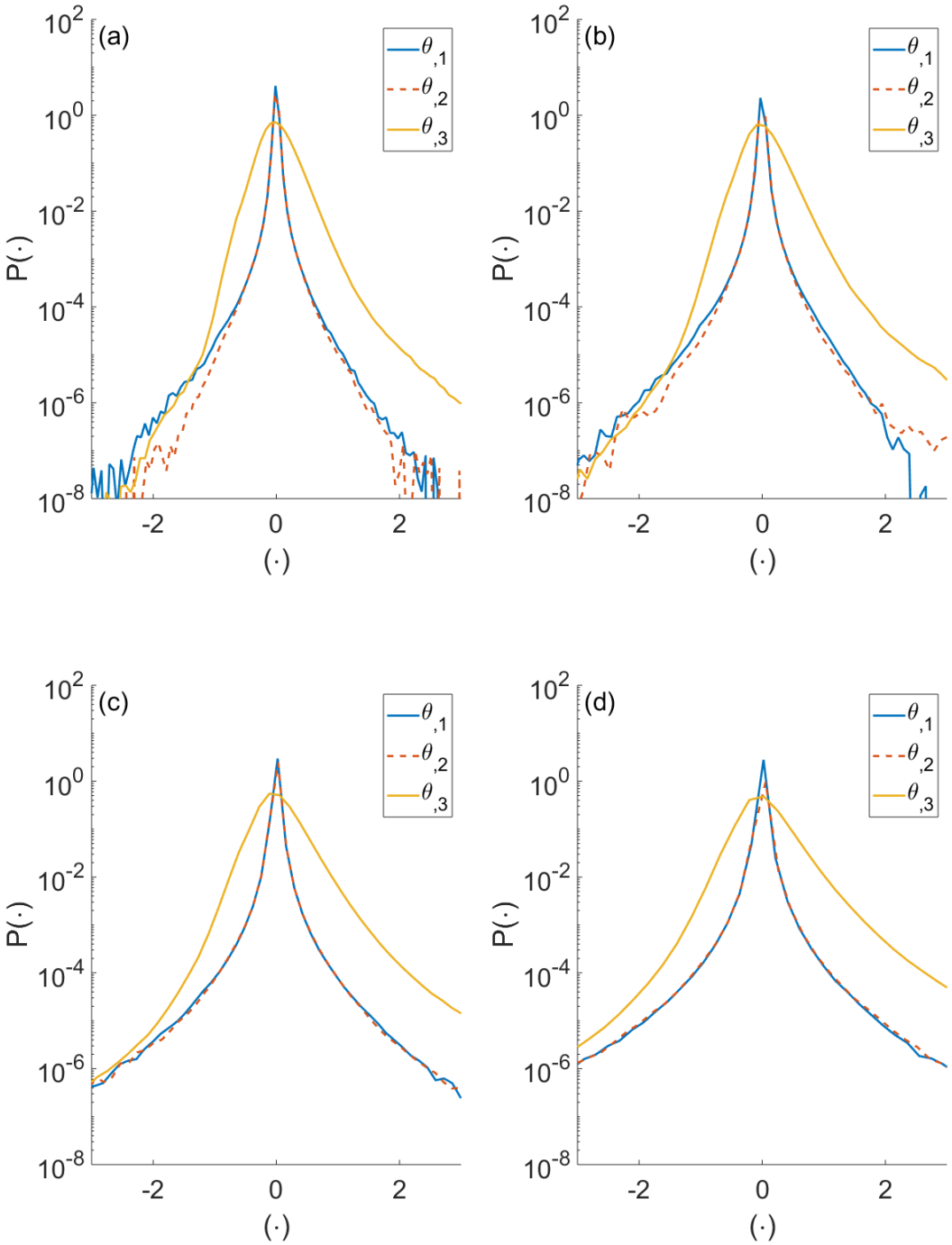

Figure 3.28: Temperature derivative p.d.f.s for N=0.6 with (a) Pr=0.7, (b) Pr=1, (c) Pr=2, and (d) Pr=4.

3.3.2 Velocity derivatives

Figures 3.15-3.18 show the effect of Pr on the velocity derivative p.d.f.s in each case of N. Figures 3.19-3.22 show the velocity derivative p.d.f.s at a fixed N for each Pr to compare the shapes of $u_{i,j}$ within each simulation. The effect of increased stratification can be seen going from Fig. 3.19 to Fig. 3.22.

When Pr is increased, there are very small changes in the velocity derivative p.d.f.s (Figs. 3.15-3.18). The difference is minimal, but upon very close inspection the peaks lower with increased Pr, particularly in $u_{3,1}$ and $u_{3,3}$ (Figs. 3.17 and 3.18 respectively). This corresponds to the probability of near-zero velocity derivatives decreasing, and can be attributed to weaker thermal diffusivity acting to damp extreme values of velocity.

In Figs. 3.19-3.22, the two distinct groups of transverse ($u_{1,3}$ and $u_{3,1}$) versus longitudinal ($u_{1,1}$ and $u_{3,3}$) velocity derivative p.d.f. groups are visible, as is the loss of this distinction at stronger stratification ($N = 0.3$ and 0.6) where $u_{1,3}$ is differently-shaped than the three other derivatives. Going from panels (a)-(d) in these figures, the distinction between the two p.d.f. groups does not appear to change with Pr. This is reasonable, as the flows stay in the same regime of stratified turbulence even with different Pr: Re_b and Fr_h are approximately constant so there should be no expected change. The visible difference between transverse versus longitudinal derivative groups are reasonable, given the characteristically quasi-two-dimensional flow in both regimes of strongly stratified flow.

The statistical moments seem to be affected minimally, as in the p.d.f.s, with changes in Pr (Tables 3.2, 3.4, 3.6, and 3.8). Regarding measures of isotropy, there are no noticeable changes when increasing Pr based on the velocity derivatives. That is, the similarity within the longitudinal or transverse derivative groups do not seem to be affected with changes in Pr. Specifically, the identification of 2 variance groups (longitudinal versus transverse) at weak stratification versus the 3 variance groups at strong stratification as in de Bruyn Kops [2015]. In the longitudinal group, the ratios of variances $u_{3,3}/u_{1,1}$ and $u_{3,3}/u_{2,2}$ are almost unchanged with increased Pr and $u_{3,3}$ is always the largest of the three.

The skewnesses and kurtoses do not appear to change significantly with Pr, though there is a clear difference between longitudinal derivatives $u_{3,3}$ and the $u_{1,1}$ and $u_{2,2}$ pair in both measurements. There are no identifiable patterns in skewness or kurtosis when Pr is changed. The symmetry of the velocity derivative distributions and proneness to outliers is seemingly unchanged whether viscosity or buoyancy diffusivity is the dominant damping process. Although the kinetic energy spectra in Sec. 3.2.1 showed sensitivity to Pr at small scales, this did not result in any enhanced isotropy in the velocity component derivatives.

3.3.3 Temperature derivatives

Figures 3.23-3.24 show the effect of Pr on the temperature derivative p.d.f.s in each case of N. Figures 3.25-3.28 show the temperature derivative p.d.f.s at a fixed N for each Pr to compare the shapes of $\theta_{,j}$ within each simulation. The effect of increased stratification can be seen going from Fig. 3.25 to Fig. 3.28.

It should be expected that the behaviours of the velocity and temperature fields will be far different once Pr takes on value different from 1. When Pr is increased, there is a significant change in all the temperature derivative p.d.f.s (Figs. 3.23-3.24): the p.d.f. shapes appear to flatten as their peaks lower and tails become much heavier, which is reflected in the kurtoses of all scalar derivatives increasing appreciably (Tables 3.3, 3.5, 3.7, and 3.9). This is also seen in fixed stratification strength groups (Figs. 3.25-3.28) where all the p.d.f.s appear to flatten in the same way as above. The peaks of the p.d.f.s drop but are still grouped in terms of horizontal ($\theta_{,1}, \theta_{,2}$) and vertical derivatives ($\theta_{,3}$). At fixed stratification strength, the p.d.f.s maintain the difference in probability of near-zero values as Pr is changed. Figure 3.24 show that the temperature derivatives take on more extreme values with lower N – this could be interpreted as less effective damping of the scalar so that larger fluctuations are more frequent. It is also shown that the temperature derivatives take on more extreme values with lower N, which can be interpreted as less effective damping of the scalar, permitting more frequent and larger fluctuations in temperature.

The moments of the temperature derivatives very much depend on Pr, as shown in Tables 3.3, 3.5, 3.7 and 3.9. There are significant changes in variances and kurtoses as Pr is increased, as expected from the p.d.f.s above. The variances show that vertical scalar derivatives will tend to take on more extreme values than horizontal derivatives. This is expected, since vertical derivatives are dominant when pancake eddies shear against each other in stratified turbulence. Higher Pr, however, seems to have a negligible effect on the difference between these horizontal and vertical variances (approximately the same ratios $\theta_{,3}/\theta_{,1}$ and $\theta_{,3}/\theta_{,2}$ are maintained).

The nonzero skewnesses of scalar derivatives parallel to the mean gradient still identify anisotropy at small scales, as expected for stratified flows [Gibson et al., 1970, de Bruyn Kops, 2015]. However, there is no identifiable pattern in the change in isotropy in terms of statistical interchangeability observed in the statistical moments (nor in the values themselves when increasing Pr).

Chapter 4

Conclusions

Direct numerical simulations of stratified turbulence were performed to study the effect of varying Pr and to investigate the soundness of the commonly used $Pr = 1$ simplification. The simulations presented here employed random forcing of large-scale vortical modes on cubic domains. A fixed viscosity and a set of N were chosen to obtain a range of Re_b and Fr_h as Pr was varied. Spectra of kinetic energy, potential energy, buoyancy flux, kinetic energy flux, and potential energy flux were examined in fixed-N groups to identify scale-specific results dependent on Pr. Snapshots of the velocity, vorticity, and temperature fluctuation and dissipation fields in physical space were also visualized for a qualitative analysis of Pr-dependence.

When varying Pr, changes were naturally expected at very small scales, which is consistent with the change in k_θ (k_d was nearly unchanged by Pr due to the fixed viscosity). Indeed, the most obvious Pr-dependence in the kinetic and potential energy spectra was found at large wavenumbers, where the potential, and perhaps surprisingly, kinetic energy grew with Pr. The increase in energy can be explained by larger Pr permitting a wider wavenumber range of temperature fluctuations, possibly excited by enhanced inter-layer instabilities, which influence both kinetic and potential energy before viscous dissipation or buoyancy diffusion can occur. Since k_d was not changed much by Pr, the spectra of kinetic energy (and kinetic energy flux) were much less affected than potential energy (and potential energy flux). Subtle changes in the physical fields were found for different Pr, except of course in the temperature fluctuation dissipation field (Fig. 3.14). This was not unexpected, as Re_b was only slightly changed for a fixed N, so no change to the transition between stratified turbulence regimes was incurred by varying Pr.

Surprisingly, Pr-dependence was found upscale of the dissipation range in most of the

examined spectra. In some cases, this even extended upscale into the large-scale forcing interval, particularly in the horizontal wavenumber spectrum. Intermediate-to-large-scale Pr-dependence was visible more in the potential energy than kinetic energy spectra. In the spectral kinetic energy flux, Pr-dependence was peculiar in that it only applied to k_h and k_v between the forcing interval and the dissipation range, where an inertial range could have existed if Re and/or Re_b were larger in these simulations. The spectral potential energy flux was extremely sensitive to Pr for most of the wavenumber range. The buoyancy flux spectra showed the strongest sensitivity to Pr in the restratification range just before k_d and k_θ, but also exhibited some N-dependence. Following the description by Holloway [1988], it could be that for large Pr, the increased abundance of potential energy at these small scales even further amplifies the conversion back to kinetic energy.

Among all the examined spectra, the $N = 0.6$ cases were very different from the three weaker stratifications. The simulations with $N = 0.6$ were the only cases in the $Re_b < 1$ regime; some of these observed differences may be consequences of the flow's transition to viscously coupled non-turbulent layers. Breaks in the horizontal kinetic and potential energy spectra occurred at k_b associated with the suppression of the downscale energy cascade in this regime. The horizontal buoyancy flux spectra in Fig. 3.10(g) showed that the forcing scales were most affected by Pr, rather than the restratification range. In the spectral energy fluxes, $N = 0.6$ was unique in that $\Pi_K(k_h)$ was affected by Pr only at intermediate-to-large scales, and both $\Pi_P(k_h)$ and $\Pi_P(k_v)$ showed Pr-dependence for most of the wavenumber range. The $N = 0.6$ cases also exhibited negative horizontal kinetic energy flux at large scales, implying an upscale transfer of energy when stratification is especially strong. None of $\Pi_K(k_h)$, $\Pi_K(k_v)$, $\Pi_P(k_h)$, nor $\Pi_P(k_v)$ displayed any discernable range of constant flux at any N (except possibly $\Pi_K(k_v)$ at $N = 0.6$). The development of a true inertial range may have been hindered by the small Re and especially Re_b.

Given the impact of Pr upscale of the dissipation range, the $Pr = 1$ simplification for modelling realistic $Pr > 1$ flows appears to be unrealistic. Depending on N, Pr was shown to affect the examined spectra with varied severity and at unexpected scales. In particular, the spectral potential energy flux was especially sensitive to Pr, and was affected over more of its wavenumber range. For any investigation that might be reliant on accurately measured potential energy transfer, special care should be taken by properly computing these quantities with the appropriate Pr if possible.

The exhibited shallowing of energy spectra with increasing Pr was consistent with the results in Okino and Hanazaki [2017]. Further, in all the examined quantities it was suggested there could be convergence to a limiting spectra shape as Pr increases, as there was a declining growth in each spectra with larger Pr. That is, for Pr larger than 8 (but not extremely large as in Okino and Hanazaki [2017]), and for large scales down to about

k_d, it is expected that these examined spectra could converge to a shape not too different from the $Pr = 8$ case. Since varying Pr result in different k_θ, it may only be at larger scales that convergence is possible. The kinetic energy and spectral kinetic energy flux did not exhibit major dependence on Pr, so using $Pr = 1$ may be acceptable for those instances when large-scale kinetic energy is the main focus. However, the potential energy, buoyancy flux, and spectral potential energy flux might not exhibit similarly close convergence until a much larger $Pr > 8$. Performing simulations with an accurate Pr may be crucial to reliably study these quantities if Pr is not extremely large.

The work in de Bruyn Kops [2015] analyzed strongly stratified turbulence simulations with $Pr = 1$ to investigate their agreement with classical KOC scaling arguments, local isotropy theory, local dissipation rates, and local intermittency theory. The analysis of velocity and temperature derivative p.d.f.s and moments for local isotropy (specifically, Sec. 3 in de Bruyn Kops [2015]) was extended upon here by studying simulations with Pr different from 1.

As demonstrated in Sec. 3.3.1, changing Pr affected the temperature derivative p.d.f.s and statistics more than the velocity derivatives which were comparatively unchanged. Larger Pr resulted in the flattening of temperature p.d.f.s, corresponding to more outlier-prone temperature derivatives in both horizontal and vertical directions. Considering de Bruyn Kops [2015]'s comparison of stratification's effect on temperature versus velocity derivative fields, it was found that changing Pr produced the opposite outcome. While a change in stratification strength produced major effects on the velocity derivatives and minor effects on the temperature derivatives, changing Pr resulted in major effects on the temperature derivatives and minor effects on the velocity derivatives. Although the temperature statistics were significantly changed with Pr, there was no identifiable change in isotropy in either the temperature or velocity derivatives.

Additional simulations with $Pr > 8$ should be considered to further explore the extent of the predicted convergence in all of the observed spectra, but would demand a higher resolution than $n = 1536$ used here. While this resolution was sufficient to bring about detectable changes between the $Pr = 4$ and $Pr = 8$ cases, the $Pr = 8$ simulations had $k_{max}/k_\theta \approx 0.7$. A wider range of Re_b as well as larger-Re simulations would allow for cases with identifiable inertial ranges to be studied. It may be of interest to explore any effects due to Pr on constant flux ranges, and to also see how restratification in the buoyancy flux spectra might change with more diverse cases. However, the original challenge still remains: attainable values of Pr, Re, and Re_b will be limited by the available computational resources. For example, to perform a simulation with $Pr = 100$ with this setup, it is estimated that a resolution of $n \approx 9700$ would be needed for $k_{max}/k_\theta \approx 0.7$, and $k_{max}/k_\theta = 1$ would need $n \approx 14000$.

For the work on p.d.f.s, statistics, and isotropy in particular, in order to properly compare $Pr \neq 1$ results to the findings in de Bruyn Kops [2015], a higher resolution than $8192 \times 8192 \times 4096$ would be needed to accommodate values of Re_b as large as theirs. Longer integration lengths and more frequent physical field output files in each simulation could have made for improved time-averaged results. Another inconsistency with de Bruyn Kops [2015] was that the p.d.f.s were not normalized in the same way. Their p.d.f.s were possibly normalized by the standard deviation, but normalization by both the mean and standard deviation were mentioned in each plot's caption. For a more complete comparison to the model paper, the rest of the topics in de Bruyn Kops [2015] could have been explored for Pr-dependence, e.g. Kolmogorov-Obukhov-Corrsin scaling, local dissipation rates and suitability of the lognormal model, internal intermittency and its coefficients.

Future work on Pr-dependence of stratified turbulence could include the effects of rotation, which were neglected here. Based on the exhibited Pr-dependence of the buoyancy flux, the effect of Pr on mixing efficiency may be an interesting extension of the work here. Exploring the very small scales and looking into possible changes in intermittency due to Pr is also of interest. The forced simulations presented here were varied in a limited way (only N and Pr were changed), but the code which produced them has many options to investigate stratified turbulence with different configurations. For example, one option could be to force fields other than the large vortical modes as shown here (e.g. velocity or temperature, possibly forcing large-scale gravity waves), or modify some of the other forcing parameters.

References

S. Almalkie and S. M. de Bruyn Kops. Kinetic energy dynamics in forced, homogeneous, and axisymmetric stably stratified turbulence. *Journal of Turbulence*, 13(29):1–32, 2012.

P. Bartello and S. M. Tobias. Sensitivity of stratified turbulence to the buoyancy Reynolds number. *Journal of Fluid Mechanics*, 725:1–22, 2013.

G. K. Batchelor. Small-scale variation of convected quantities like temperature in turbulent fluid Part 1. General discussion and the case of small conductivity. *Journal of Fluid Mechanics*, 5(1):113–133, 1959.

P. Billant and J.-M. Chomaz. Self-similarity of strongly stratified inviscid flows. *Physics of Fluids*, 13(6):1645–1651, 2001.

G. Brethouwer, P. Billant, E. Lindborg, and J.-M. Chomaz. Scaling analysis and simulation of strongly stratified turbulent flows. *Journal of Fluid Mechanics*, 585:343–368, 2007.

J. M. Burgers. A mathematical model illustrating the theory of turbulence. In R. von Mises and T. von Kármán, editors, *Advances in Applied Mechanics*, volume 1, pages 171–199. Elsevier, 1948.

G. F. Carnevale, M. Briscolini, and P. Orlandi. Buoyancy-to inertial-range transition in forced stratified turbulence. *Journal of Fluid Mechanics*, 427:205–239, 2001.

S. Corrsin. On the spectrum of isotropic temperature fluctuations in an isotropic turbulence. *Journal of Applied Physics*, 22(4):469–473, 1951.

P. A. Davidson. *Turbulence in Rotating, Stratified and Electrically Conducting Fluids*. Cambridge University Press, 2013.

P. A. Davidson. *Turbulence: An Introduction for Scientists and Engineers*. Oxford University Press, 2015.

S. M. de Bruyn Kops. Classical scaling and intermittency in strongly stratified Boussinesq turbulence. *Journal of Fluid Mechanics*, 775:436–463, 2015.

M. B. de Stadler, S. Sarkar, and K. A. Brucker. Effect of the Prandtl number on a stratified turbulent wake. *Physics of Fluids*, 22(9):095102, 2010.

E. M. Dewan. Saturated-cascade similitude theory of gravity wave spectra. *Journal of Geophysical Research: Atmospheres*, 102(D25):29799–29817, 1997.

D. R. Durran. *Numerical Methods for Fluid Dynamics: With Applications to Geophysics*, volume 32 of *Texts in Applied Mathematics*. Springer, 2010.

M. Frigo and S. G. Johnson. The design and implementation of FFTW3. *Proceedings of the IEEE*, 93(2):216–231, 2005.

T. Gerz, U. Schumann, and S. E. Elghobashi. Direct numerical simulation of stratified homogeneous turbulent shear flows. *Journal of Fluid Mechanics*, 200:563–594, 1989.

C. H. Gibson. Fossil temperature, salinity, and vorticity turbulence in the ocean. In J. C. J. Nihoul, editor, *Marine Turbulence*, volume 28 of *Elsevier Oceanography Series*, pages 221–257. Elsevier, 1980.

C. H. Gibson, G. R. Stegen, and S. McConnell. Measurements of the universal constant in Kolmogoroff's third hypothesis for high Reynolds number turbulence. *Physics of Fluids*, 13(10):2448–2451, 1970.

T. Gotoh and P. K. Yeung. Passive scalar transport in turbulence: a computational perspective. In P. A. Davidson, Y. Kaneda, and K. R. Sreenivasan, editors, *Ten Chapters in Turbulence*, pages 87–131. Cambridge University Press, 2013.

J. R. Herring and O. Métais. Numerical experiments in forced stably stratified turbulence. *Journal of Fluid Mechanics*, 202:97–115, 1989.

G. Holloway. The buoyancy flux from internal gravity wave breaking. *Dynamics of Atmospheres and Oceans*, 12(2):107–125, 1988.

T. Ishihara, Y. Kaneda, and J. C. R. Hunt. Thin shear layers in high Reynolds number turbulence DNS results. *Flow, Turbulence and Combustion*, 91(4):895–929, 2013.

A. N. Kolmogorov. The local structure of turbulence in incompressible viscous fluid for very large Reynolds numbers. *Doklady Akademii Nauk SSSR*, 30:301–305, 1941.

A. N. Kolmogorov. A refinement of previous hypotheses concerning the local structure of turbulence in a viscous incompressible fluid at high Reynolds number. *Journal of Fluid Mechanics*, 13(1):82–85, 1962.

P. K. Kundu, I. M. Cohen, and D. R. Dowling. *Fluid Mechanics*. Academic Press, 5th edition, 2012.

C. J. Lang and M. L. Waite. Scale-dependent anisotropy in forced stratified turbulence. *Physical Review Fluids*, 4(4):044801, 2019.

J.-P. Laval, J. C. McWilliams, and B. Dubrulle. Forced stratified turbulence: Successive transitions with Reynolds number. *Physical Review E*, 68(3):036308, 2003.

D. K. Lilly. Stratified Turbulence and the Mesoscale Variability of the Atmosphere. *Journal of the Atmospheric Sciences*, 40(3):749–761, 1983.

E. Lindborg. The energy cascade in a strongly stratified fluid. *Journal of Fluid Mechanics*, 550:207–242, 2006.

D. Lucas, C. C. P. Caulfield, and R. R. Kerswell. Layer formation in horizontally forced stratified turbulence: connecting exact coherent structures to linear instabilities. *Journal of Fluid Mechanics*, 832:409–437, 2017.

A. Maffioli. Vertical spectra of stratified turbulence at large horizontal scales. *Physical Review Fluids*, 2(10):104802, 2017.

A. Maffioli and P. A. Davidson. Dynamics of stratified turbulence decaying from a high buoyancy Reynolds number. *Journal of Fluid Mechanics*, 786:210–233, 2016.

P. Moin and K. Mahesh. Direct numerical simulation: A tool in turbulence research. *Annual Review of Fluid Mechanics*, 30:539–578, 1998.

A. M. Obukhov. Spectral energy distribution in a turbulent flow. *Doklady Akademii Nauk SSSR*, 32:22–24, 1941a.

A. M. Obukhov. Spectral energy distribution in a turbulent flow. *Izvestiya Akademii Nauk SSR*, 5:453–466, 1941b.

A. M. Obukhov. Structure of temperature field in a turbulent flow. *Izvestiya Akademii Nauk SSR*, 13:58, 1949.

A. M. Obukhov. Some specific features of atmospheric turbulence. *Journal of Fluid Mechanics*, 13(1):7781, 1962.

S. Okino and H. Hanazaki. Turbulence in a fluid stratified by a high Prandtl-number scalar. In M. Resch, W. Bez, E. Focht, M. Gienger, and H. Kobayashi, editors, *Sustained Simulation Performance 2017*, pages 113–121. Springer, 2017.

R. V. Ozmidov. On the turbulent exchange in a stably stratified ocean. *Izvestiya Akademii Nauk SSR*, 1:861–871, 1965.

L. F. Richardson. *Weather Prediction by Numerical Process*. Cambridge University Press, 1922.

J. J. Riley and S. M. de Bruyn Kops. Dynamics of turbulence strongly influenced by buoyancy. *Physics of Fluids*, 15(7):2047–2059, 2003.

J. J. Riley and M.-P. Lelong. Fluid motions in the presence of strong stable stratification. *Annual Review of Fluid Mechanics*, 32(1):613–657, 2000.

J. J. Riley and E. Lindborg. Recent progress in stratified turbulence. In P. A. Davidson, Y. Kaneda, and K. R. Sreenivasan, editors, *Ten Chapters in Turbulence*, pages 269–317. Cambridge University Press, 2013.

H. A. Rose and P. L. Sulem. Fully developed turbulence and statistical mechanics. *Journal de Physique*, 39(5):441–484, 1978.

E. D. Siggia. Numerical study of small-scale intermittency in three-dimensional turbulence. *Journal of Fluid Mechanics*, 107:375–406, 1981.

L. M. Smith and F. Waleffe. Generation of slow large scales in forced rotating stratified turbulence. *Journal of Fluid Mechanics*, 451:145–168, 2002.

C. Staquet and J. Sommeria. Internal gravity waves: from instabilities to turbulence. *Annual Review of Fluid Mechanics*, 34(1):559–593, 2002.

G. I. Taylor. Statistical theory of turbulence. *Proceedings of the Royal Society of London, Series A*, 151(873):421–444, 1935.

H. Tennekes and J. L. Lumley. *A First Course in Turbulence*. MIT press, 1972.

D. J. Tritton. *Physical Fluid Dynamics*. Oxford University Press, 2nd edition, 1988.

M. L. Waite. Stratified turbulence at the buoyancy scale. *Physics of Fluids*, 23(6):066602, 2011.

M. L. Waite. Potential enstrophy in stratified turbulence. *Journal of Fluid Mechanics*, 722, 2013.

M. L. Waite. Direct Numerical Simulations of Laboratory-Scale Stratified Turbulence. In *Modeling Atmospheric and Oceanic Flows: Insights from Laboratory Experiments and Numerical Simulations*, chapter 8, pages 159–175. American Geophysical Union, 2014.

M. L. Waite. Random forcing of geostrophic motion in rotating stratified turbulence. *Physics of Fluids*, 29(12):126602, 2017.

M. L. Waite and P. Bartello. Stratified turbulence dominated by vortical motion. *Journal of Fluid Mechanics*, 517:281–308, 2004.

J. C. Wyngaard. *Turbulence in the Atmosphere*. Cambridge University Press, 2010.